cm CHEMISTRY OF MATERIALS

OCTOBER 13, 2015 | VOLUME 27 | NUMBER 19 | pubs.acs.org/cm

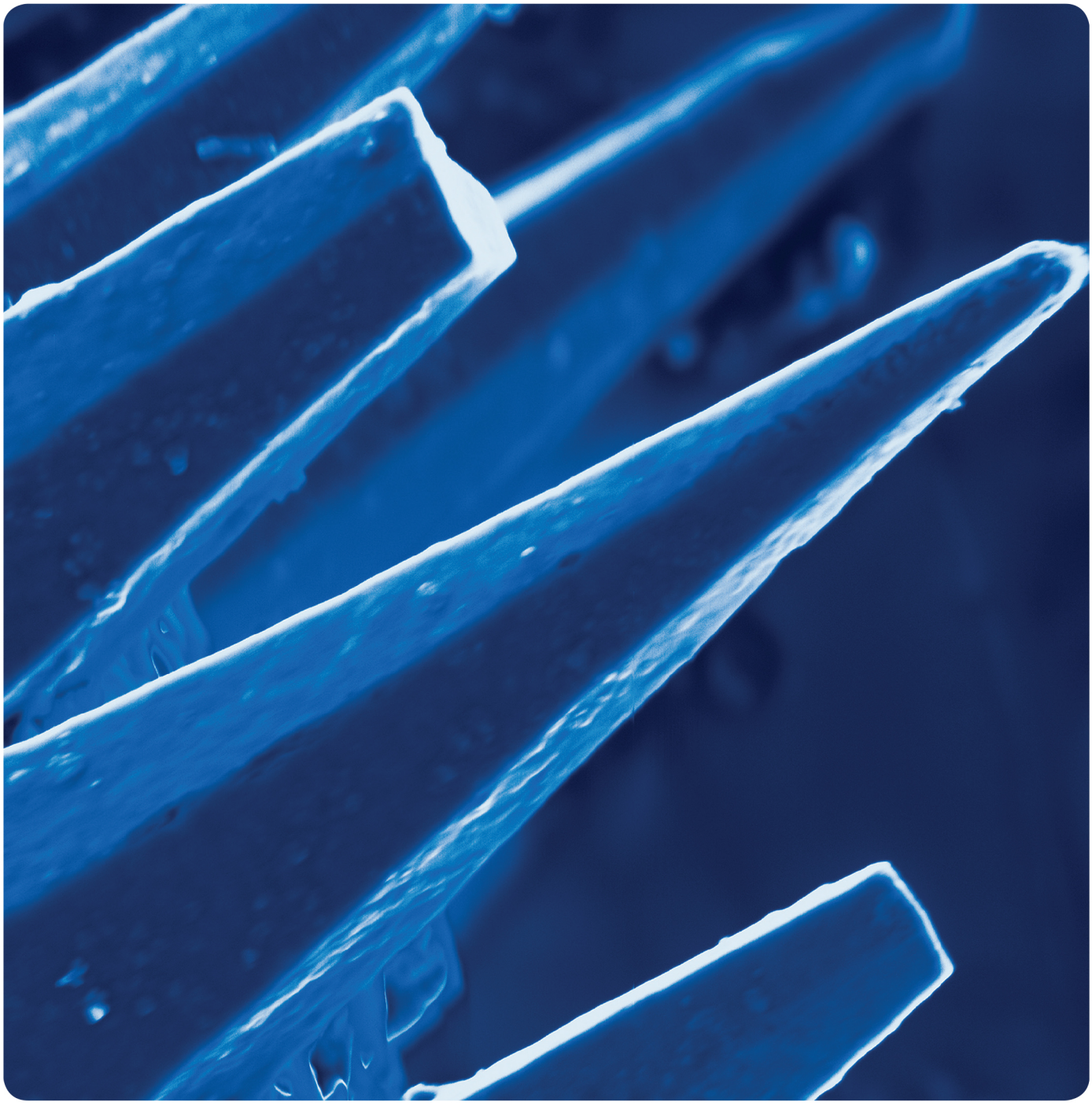

ACS Publications
Most Trusted. Most Cited. Most Read.

www.acs.org

CHEMISTRY OF MATERIALS

Article

pubs.acs.org/cm

Narrowly Distributed Crystal Orientation in Biomineral Vaterite

Boaz Pokroy,[†] Lee Kabalah-Amitai,[†] Iryna Polishchuk,[†] Ross T. DeVol,[‡] Adam Z. Blonsky,[‡] Chang-Yu Sun,[‡] Matthew A. Marcus,[§] Andreas Scholl,[§] and Pupa U.P.A. Gilbert*[,‡,∥,⊥,▽]

[†]Department of Materials Science & Engineering and the Russell Berrie Nanotechnology Institute, Technion - Israel Institute of Technology, Haifa 32000, Israel

[‡]Department of Physics, University of Wisconsin—Madison, 1150 University Avenue, Madison, Wisconsin 53706, United States

[§]Advanced Light Source, Lawrence Berkeley National Laboratory, 1 Cyclotron Road, Berkeley, California 94720, United States

[∥]Department of Chemistry, University of Wisconsin—Madison, 1101 University Avenue, Madison, Wisconsin 53706, United States

[⊥]Radcliffe Institute for Advanced Study, Harvard University, 8 Garden Street, Cambridge, Massachusetts 02138, United States

Supporting Information

ABSTRACT: Biominerals formed by animals provide skeletal support and many other functions. They were previously shown to grow by aggregation of amorphous nanoparticles but never to grow ion-by-ion from solution, which is a common growth mechanism for abiotic crystals. We analyze vaterite ($CaCO_3$) multicrystalline spicules from the solitary tunicate Herdmania momus, with polarization-dependent imaging contrast (PIC)-mapping and scanning and aberration-corrected transmission electron microscopies. The first fully quantitative PIC-mapping data, presented here, measured 0-30° angle spreads between immediately adjacent crystals. Such narrowly distributed crystal orientations demonstrate that crystallinity does not propagate from one crystal to another (0° angle spreads), nor that new crystals with random orientation (90°) nucleate. There are no organic layers at the interface between crystals; hence, a new, unknown growth mechanism must be invoked, with crystal nucleation constrained within 30°. Two observations are consistent with crystal growth from solution: vaterite microcrystals express crystal faces and are smooth at the nanoscale after cryo-fracture. The observation of 30° angle spreads, lack of interfacial organic layers, and smooth fracture figures broadens the range of known biomineralization mechanisms and may inspire novel synthetic crystal growth strategies. Spherulitic growth from solution is one possible mechanism consistent with all these observations.

INTRODUCTION

Biominerals are polycrystalline minerals formed by living organisms, with a multitude of functions, including skeletal support,[1] locomotion, biting,[2] mastication,[3] attack and defense tools,[4] gravity and magnetic field sensing,[5,6] and many others.[7] Biominerals nearly always include intra- and intercrystalline organic molecules,[8] even when pathological mineralization occurs,[9,10] and at the end of their diverse formation mechanisms they result in hard and tough tissues with varying degrees of crystal co-orientation: from the single-crystalline sea urchin spicules and spines to randomly oriented polycrystalline aragonite in the outer part of Nautilus shells. Bone, teeth, and various mollusc and brachiopod shell structures all have intermediate crystal orientation angle spreads.[11−19]

Rarely do organisms utilize vaterite ($CaCO_3$) as their mineral components,[7,20] possibly because vaterite is more soluble and less stable than calcite and aragonite (both also $CaCO_3$). One such organism is the sea squirt *Herdmania momus*,[21] a tunicate that forms vaterite spicules in its tunic and body presumably for stiffening these tissues, while maintaining a flexible structure. Its spicules exhibit a unique morphology: a series of pointy crystals arranged in a "crown of thorns" motif, which helically surround elongated core fibers. Each thorn is a larger, higher-quality single crystal than any geologic or synthetic vaterite ever observed. These thorns were therefore used recently to reveal the double-structure of vaterite: electron phase contrast imaging along the *c*-axis of a single thorn revealed a major hexagonal structure identical to the one described by Kamhi[22] (space group of *P*63/*mmc* with a = 4.13 Å and c = 8.49 Å), whereas the other minor structure has symmetry still unknown and larger crystal lattice spacing.[23,24]

In this work we investigate entire vaterite spicules from the same animal, their crystal orientations, and their formation mechanism, by using polarization-dependent imaging contrast (PIC)-mapping,[25−31] a mode of photoemission electron spectromicroscopy (PEEM),[32] and scanning and aberration corrected transmission electron microscopies (SEM and TEM).

Received: April 26, 2015
Revised: August 29, 2015
Published: August 31, 2015

DOI: 10.1021/acs.chemmater.5b01542
Chem. Mater. 2015, 27, 6516−6523

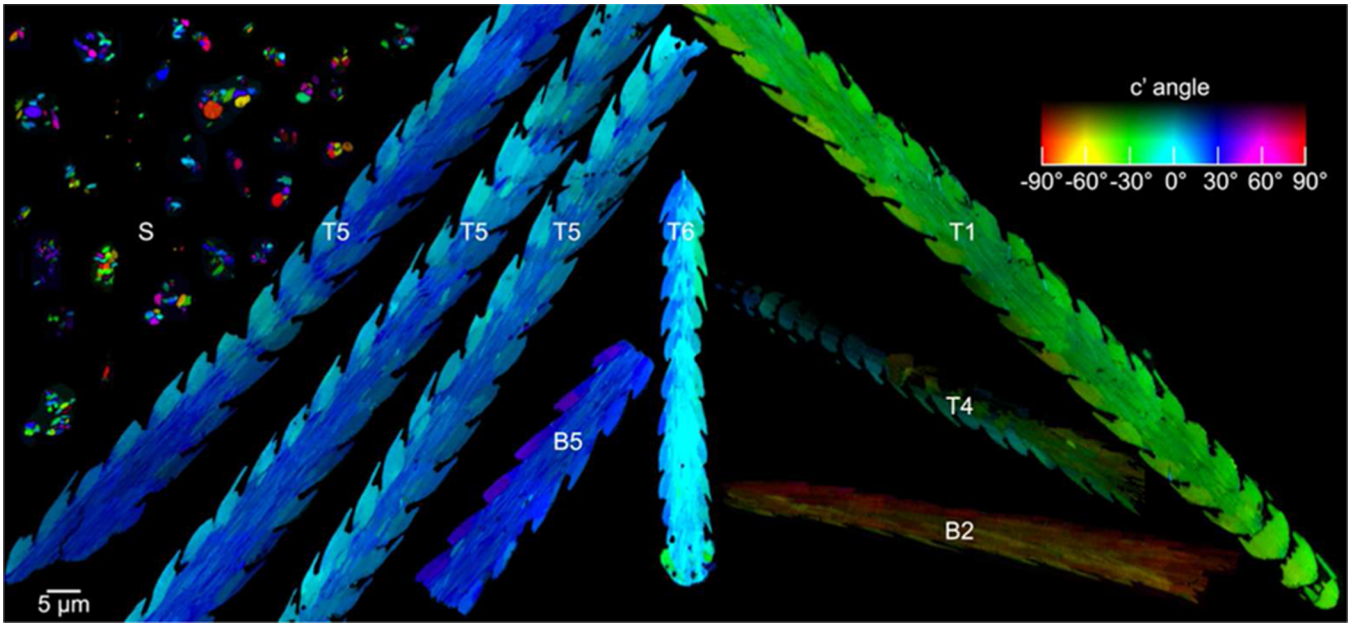

Figure 1. Composition of PIC-maps of vaterite tunic (T) and body (B) spicules from *H. momus* in polished cross-section. Color and brightness quantitatively represent the orientation of vaterite crystals and demonstrate that each spicule is multicrystalline, with small-angle branching of crystallites as shown by different but nearby colors in each spicule. Thorns, protruding from the core of each spicule, are the largest singly oriented crystals. Synthetic vaterite crystalline domains (S) are randomly oriented. Spicule T5 is segmented for efficient space use. The color bar displays in different hues different angles between the vertical and the *c*′-axis (projection of the vaterite *c*-axis onto the polarization plane, which is in turn perpendicular to the X-ray beam, and is tilted by 60° around the vertical with respect to the image plane shown here). A crystal with vertical *c*- or *c*′-axis is cyan, and the horizontal one is red. Brightness displays how far off-plane the *c*-axis is oriented. Dark crystals, e.g., in spicules T4 and B2, have their *c*-axes nearly normal to the polarization plane, and bright crystals have their *c*-axes in the polarization plane, as in spicule T6.

The TEM data also include nanobeam linescan electron diffraction.

RESULTS

Crystal Orientation Measurements. In Figure 1 we present a montage of all the vaterite spicules analyzed in this work, along with synthetic vaterite. In synthetic vaterite we observe micrometer-size domains, each of which includes many co-oriented nanoparticles, whereas domains are randomly oriented with respect to one another. Each biogenic vaterite spicule, instead, shows a small angle spread of crystal orientations, evidenced by similar colors.

In a PIC-map different colors correspond to different crystal orientations, measured based on linear dichroism,[33] an X-ray effect that makes π^* peaks in carbon and oxygen absorption spectra vary in intensity depending on the orientation of π-bonded carbonate groups. When π orbitals are parallel/perpendicular to the linear polarization of the illuminating X-ray beam, the peak has maximum/minimum intensity, respectively, because the dipole interaction is maximum/minimum. In a PIC-map this orientation sensitivity is exploited to visually display crystal orientations.

In Figure 2 we show the tip of spicule T1 physically rotated to be imaged in three different positions. They therefore provide a complete 3D quantitative description of the vaterite *c*-axis orientation, rather than its projection onto a 2D plane. This is the first fully quantitative measurement of the arrangement of single crystals in their pristine crystal orientation pattern, obtained with 20 nm resolution. Figure S1 shows a level-enhanced, nonquantitative version of Figure 2, to display vaterite crystals, even in the positions in which one can hardly see them in Figure 2.

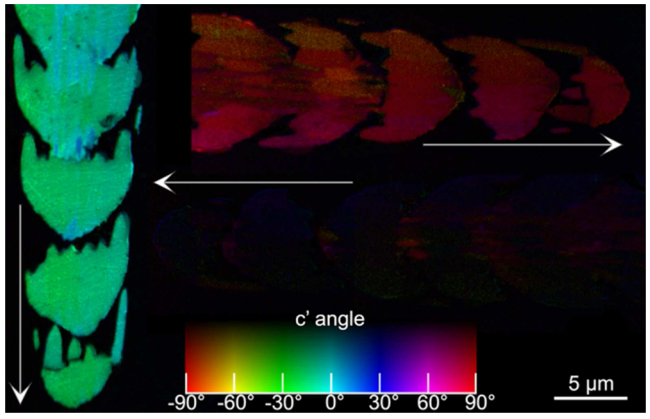

Figure 2. PIC-maps of one spicule (T1 in Figure 1) imaged after physically rotating the sample. In all three PIC-maps the arrows point toward the tip of the spicule. In the vertical position the crystals are blue−cyan−green, indicating vertical or nearly vertical *c*′- and *c*-axes. When the spicule is rotated horizontally, therefore, the colors become orange−red−magenta to indicate a general horizontal direction of *c*′-axes. In the horizontal positions the crystals are darker as expected, because the image plane is 60° from the polarization plane. In addition, the two horizontal positions are different from one another: the left-pointing spicule is almost completely black, indicating that the c-axes of its crystals are not in the image plane but 30° off-plane, perpendicular to the polarization plane; that is, they point straight into the incident X-ray beam. See Figure S1 for a brighter version of this figure.

In Table 1 we present the measured angular distances between the *c*′-axes and *c*-axes in pairs of adjacent crystals. Crystalline *c*-axes may be oriented anywhere in 3D, and their 3D orientation is measured, whereas *c*′-axes are projected onto

DOI: 10.1021/acs.chemmater.5b01542
Chem. Mater. 2015, 27, 6516−6523

Table 1. Angular Distances for Crystals in the Spicule of Figure 2, Measured in Different Positions: Vertical or Horizontal with the Tip on the Right[a]

crystals compared	spicule orientation	$\Delta c'$ (°)	Δc (°)
1, 2	vertical	3.9	4.1
1, 2	horizontal	5.8	5.6
3, 4	vertical	3.1	3.1
3, 4	horizontal	5.1	3.3
5, 6	vertical	1.6	1.7
5, 6	horizontal	4.7	2.9
7, 8	vertical	14.8	13.6
7, 8	horizontal	20.2	16.2

[a]Crystals 1−8 are shown in Figure S2. The angular distance of two adjacent crystals is measured in two different ways: $\Delta c'$ is the angular distance of the c'-axes, thus in 2D; Δc is the angular distance of the c-axes in 3D. Rotating the spicule from vertical to horizontal yields identical measurements, within an error of 3°, for both $\Delta c'$ and Δc. Furthermore, $\Delta c'$ and Δc are within 4° of one another. See Supporting Information Sections 4.4 and 4.6 for further details and Figure S3 for a schematic showing $\Delta c'$ and Δc. In both measurements the uncertainty is 2°.[34].

the 2D polarization plane, which is 60° from the image plane, rotated around the vertical in the image, which is also the laboratory's vertical. The measured numbers are in excellent agreement with one another, because for this spicule all crystalline c-axes are nearly in the polarization plane, which is the most favorable case. In the general case, if c-axes are farther off-plane, the 3D angular distance Δc is perfectly quantitative, but the 2D $\Delta c'$ could be either larger or smaller depending on the projection angle onto the polarization plane. Notice that the disagreement in Δc between the two rotator positions is always smaller than the disagreement in $\Delta c'$, as expected.

The biogenic vaterite crystals in Figures 1 and 2 have small angle spreads, between 0° and 30°, as shown in Figure 3.

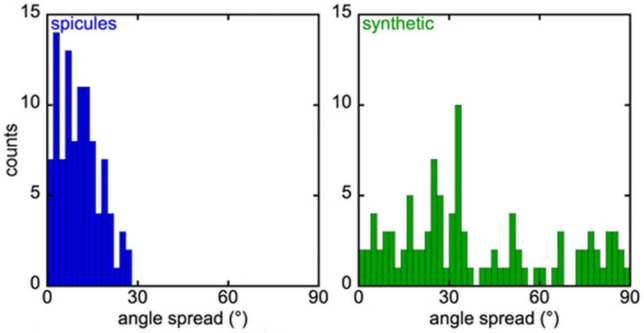

Figure 3. Histogram of angular distances $\Delta c'$ between two adjacent crystals in biogenic vaterite spicules and synthetic vaterite, measured from the PIC-maps in Figure 1. The biogenic vaterite crystals only show small angular distances (0−30°), whereas synthetic vaterite domains of nanoparticles are randomly oriented (0−90°).

In Figure 3 we show the angular distance of c'-axes across the interface of vaterite orientation domains of nanoparticles in synthetic vaterite or single crystals in spicules. Clearly the orientation within a nanoparticle domain in synthetic vaterite is most often homogeneous, but adjacent domains are randomly oriented ("S" in Figure 1 and "synthetic" in Figure 3). On the other hand vaterite spicules consistently show much smaller angular distances, less than 30°.

In Figures 4 and S4−S6 we present SEM micrographs of the core and thorns of body spicules cryo-fractured in liquid N_2 to expose their fracture figure, which is smooth and does not exhibit nanoparticles.

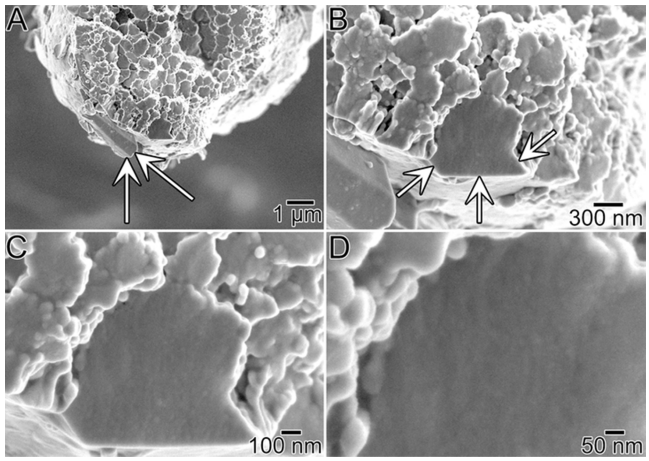

Figure 4. SEM micrographs of a cryo-fractured body spicule. No nanoparticulate texture appears in a broken thorn. Two thorns show crystalline faces (arrows in A and B) of two euhedral (hexagonal pyramid) crystals, which are more clearly visible in B and C. Notice the smooth thorn fracture figure in D. Additional thorns and core crystals are shown in Figures S4−S6.

Figures 5 and S7 show that vaterite crystals with different orientations directly abut one another, with no organics at the interface Table 2.

DISCUSSION

The data in Figures 1−3 show that individual crystallites in vaterite spicules form an elongated structure with core crystals and euhedral thorns (Figure 4), all of which are space filling, with neither voids nor organics at the interface of differently

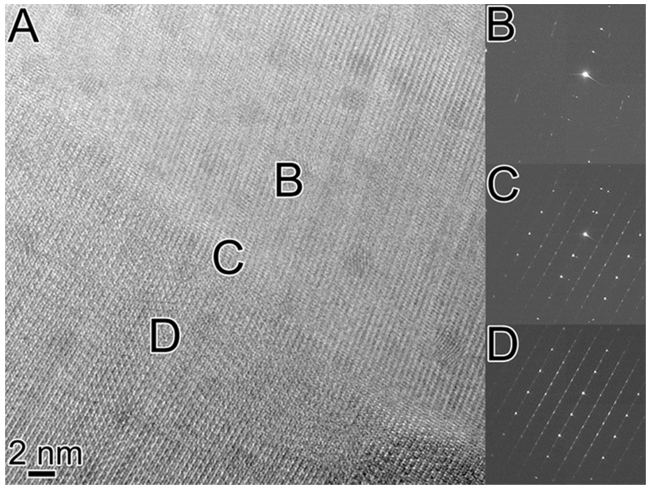

Figure 5. A. HRTEM micrograph of a portion of body spicule, including a core and a thorn crystal. B, C, D. Nanobeam linescan electron diffraction obtained with 3-nm beam from the core (B), the interface (C), and the thorn crystal (D). The two crystal lattices differ in orientation, but there are no organics or other discontinuities at their interface. The interface clearly shows reflections from both crystal lattices. Additional abutting crystals are shown in Figure S7.

DOI: 10.1021/acs.chemmater.5b01542
Chem. Mater. 2015, 27, 6516−6523

Table 2. Summary of the Techniques Used in This Work, the Parameters Each Measured, and the Main Observations Each Provided in Vaterite Spicules

technique	parameter measured	observation in spicules
PIC-mapping	orientation of crystals, 20 nm resolution	angle spreads < 30°
FIB + TEM	orientation of crystals, 2 nm resolution	angle spreads < 30°; no organics between adjacent crystals
SEM	Surface morphology	faceted thorn crystals, smooth non-nanoparticulate cryo-fractured crystals

oriented crystals (Figure 5). These crystallites have narrowly distributed angle spreads, within 0−30° around the spicule axis; thus, all crystals in a spicule have their *c*-axes aligned with the spicule axis, not perfectly, but within ±15°.

Similar 0−30° angle spreads were previously observed in nacre,[19] where aragonite ($CaCO_3$) crystalline tablets are separated by organic sheets everywhere, except in Checa bridges.[35,36] In materials science, interfaces between crystals with similar but usually smaller mis-orientation angles, on the order of 15° and below, are termed "low angle grain boundaries" or "mosaicity".[37−39]

The observed angle spreads of 0°-30° make vaterite spicules different from single crystals, either bulk or branched as snowflakes, and from fractal crystal growth, where adjacent crystals are randomly oriented. They likely correspond to low angle boundaries, which have been observed in many materials with high degree of crystallinity, including metals, ceramics, minerals, and molecular crystals.[39] The lack of organics at crystal interfaces, shown in Figure 5 and Figure S7, corroborates this interpretation.

Crystals growing with low-angle branching (e.g., 30°) were previously observed and termed "non-crystallographic branching", in spherulitic crystals.[40−42] "Spherulitic crystal growth" is defined as radial polycrystalline growth resulting from successive noncrystallographic branching (NCB) from a central nucleus.[40,43] The vaterite spicules presented here clearly do not resemble spheres and do not exhibit the radially distributed acicular crystals that in spherulites appear at all angles, starting from a single center. However, locally the vaterite crystals in each spicule may be interpreted as a small-angle sector of a spherulite, in which the centers of radially distributed crystals move along the spicule axis as the spicule grows, making this a feather-like or "plumose" spherulite.[44] The present data do not demonstrate spherulitic growth, because low-angle branching of crystals is necessary but not sufficient to identify spherulitic growth. Hence other mechanisms, distinct from spherulitic growth, may produce nucleation of crystals with lattices at 0−30° angle spreads, on the surface of previous crystals.

Adjacent crystals are always space-filling[45] and directly abut one another inside the spicule, at either end of each spicule and along its length. They were therefore never observed to form with the morphology of branches or dendrites; hence, the term "branching" does not seem appropriate to describe crystal lattices tilted by a 0−30° angle from one another.

Spherulitic growth is observed most frequently in crystals formed ion-by-ion from solution,[40] in sulphates,[46,47] carbonates,[48,49] and oxalates,[50] or via phase-transformation, for instance in the case of glass to crystalline phase, e.g., in small organic molecules,[51,52] or crystallization of polymers from the melt, e.g., in plastics[53] or metals.[53,54] If vaterite spicules grow spherulitically, it is conceivable, therefore, that they either grow by attachment of amorphous precursor particles and solid-state transformation to crystalline vaterite, as indicated by the Wolf group in in vitro studies,[55] or grow ion-by-ion from solution. We attempted to distinguish between these two possibilities with SEM experiments. In Figures 4, S4, and S5 we noticed that the fracture figure of vaterite crystals is smooth and does not exhibit nanoparticles. The presence of nanoparticulate fracture demonstrates growth by particle attachment; its absence, however, does not rule it out. Crystal growth from solution is a possible interpretation of smooth crystal fracture.

Figure S8 shows a typical cryo-fracture figure of a sea urchin spicule, which does form by aggregation of amorphous precursor nanoparticles[56] and fractures accordingly.[56,57] We only know the formation mechanisms of a few biominerals, but for all those cases, nanoparticulate fracture is a shared character.[58−61]

The smooth fracture figures of core crystallites and thorns in spicules suggest that these vaterite crystals may not have grown nanoparticle-by-nanoparticle[60] but ion-by-ion from solution or by aggregation of particles followed by dissolution and reprecipitation. Additional evidence consistent with the possibility of ion-by-ion crystal growth is provided by the crystal faces observed in vaterite spicule thorns (Figures 4 and S6). Such euhedral crystals, with flat faces and sharp corners, are rarely observed in mature, eukaryotic biominerals forming via amorphous precursors. They have been observed in biominerals formed by unknown mechanisms in unicellular organisms[62,63] and in only two other animal biominerals: (i) the limpet radula teeth, which are made of goethite, show crystal faces common in synthetic and geologic goethite, and appear to form from solution;[64] and (ii) enamel hexagonal nanorods, which form via an amorphous precursor at first,[65] and then overgrowth is from solution.[66] Observation of euhedral crystals in vaterite spicules may therefore indicate that these crystals grew from solution. Again this is not conclusive proof, simply an indication, which in our opinion is stronger than the smooth fracture. Furthermore, the two separate and independent indications, smooth fracture and faceted crystal morphology, strengthen one another.

The ion-by-ion crystal growth suggested by Figures 4 and S4−S6 does not exclude that amorphous nanoparticles were *initially* delivered to the mineralization site. If such particles were present, they may have undergone dissolution and reprecipitation; thus, only the *final stage* of crystal formation was via ion-by-ion growth from solution. This is the case in synthetic vaterite growth, which starts from amorphous calcium carbonate that rapidly dissolves and reprecipitates as vaterite.[67]

Finally, Figures 5 and S7 show that vaterite crystals with different orientations directly abut one another, with no organics at the interface. This is also unusual for biominerals and typical of polycrystalline materials growing abiotically.[68]

All these independent lines of evidence concur to demonstrate that vaterite spicules are most unusual among eukaryotic biominerals and may point in the direction of possible growth mechanisms, which remain to be demonstrated. Such mechanisms are strongly constrained by the present observation of crystals nucleating within 0−30° angle spreads and immediately abutting other crystals.

If the spicules grow from solution, we see, among others, three possible scenarios: (1) The whole spicule is one single crystal, resulting from one nucleation event, and the differently oriented crystallites result from internal or external stress

DOI: 10.1021/acs.chemmater.5b01542
Chem. Mater. 2015, 27, 6516−6523

during the crystal growth process. (2) There is a new nucleation event for each differently oriented crystallite, with similar but not identical orientation. (3) The similarity of orientation is a result of faster growth rate along the crystallographic *c*-axis and confinement in an organic compartment that does not allow the spicule to expand radially but only to grow longitudinally. The first scenario is consistent with the observation that spicules are extremely flexible when seen at the optical microscope in a droplet of ethanol as it evaporates and convects vigorously. If the spicule is bent during crystal growth, the stress could be significant, and the resulting growth strained and mis-oriented. The second and third are plausible, as in other biomineral similar mechanisms have been observed.[18,69,70]

Perhaps the most promising avenue to pursue in elucidating such formation mechanisms is a broader study of spherulitic biominerals. Many biominerals have been assumed from their morphology to be spherulitic, including corals,[71] vertebrate otoconia,[72] crustacean statoliths,[73] fish otoliths,[74,75] and avian eggshells.[76,77] Some corals show a radial distribution of crystal orientations in transmission PIC-mapping,[78] and others show random orientations in polarized light microscopy.[79] Some eggshells have randomly oriented calcite crystals and others a preferred radial orientation.[80] Only bioinduced, not biocontrolled,[7] kidney stones have been demonstrated to form spherulitically, with crystal orientation analysis.[81−84] For all other biominerals, however, there is no high-resolution quantitative analysis showing the orientations of crystals and their cryo-fracture figures. In the absence of such data it is hard to assess whether the present results are widespread or rare.

Orientation analysis will demonstrate whether or not other biominerals grow spherulitically and show differences or similarities with vaterite spicules. We stress that high-resolution PIC-mapping was necessary in order to measure the nano- and microcrystal orientations described here in vaterite spicules. Coarser resolution, however, is sufficient for quantitative crystal orientation analysis of larger biominerals, including corals and eggshells; thus narrowly distributed angle spreads can be demonstrated using X-ray diffraction, or even simple visible light microscopy with crossed polarizers. Once sufficient studies of other biominerals are completed, the significance of spherulitic biomineral growth will be clearer.

In synthetic vaterite, the morphology of crystals depends on the growth conditions evolving from hexagonal monocrystalline plates, to florets and finally to spherulites as the supersaturation increases.[85] Adding alcohol also changes the morphology of synthetic vaterite crystals.[41] Unknown, biologically controlled conditions for biomineral formation, therefore, may determine the morphology and crystal orientation patterns in vaterite biominerals, such as the spicules described here or defective vaterite mineralization in mollusk shells,[86−88] freshwater lackluster pearls,[89] green turtle eggshells,[90] and coho salmon otoliths.[91]

Few biominerals have been studied with this question in mind, but it is possible that ion-by-ion growth from solution is a widespread growth mechanism, e.g., in poorly controlled biological mineralization processes such as in calcareous algae.

The evolutionary advantage, if there is one, of making vaterite spicules, instead of calcite or aragonite, remains obscure. Among the three anhydrous polymorphs of calcium carbonate, vaterite is the most soluble, has the lowest density, has no hydrated polymorphs, and is the least thermodynamically stable, but *H. momus* masters vaterite stabilization; in fact, its spicules remain vateritic even years after extraction from the animal or a year in seawater.[21] It is possible that there exist correlations between the vaterite polymorph selection, the large crystal sizes, the 0−30° orientation angles described here, and the mechanical support function of the spicules. Future experiments will investigate possible correlations.

METHODS

Detailed methods are described in Supporting Information Detailed Methods. Briefly, vaterite spicules were extracted from *H. momus*, embedded in epoxy, polished, and coated with 1 nm Pt in the area to be analyzed by PEEM and 40 nm around it, as described in refs 28−30. PEEM experiments were done on PEEM-3[32] at the Advanced Light Source in Berkeley, CA, U.S.A. SEM and TEM experiments were done at Technion, Haifa, Israel, using a Zeiss Ultra-Plus Field Emission Gun (FEG)-SEM and an aberration-corrected Titan FEI (S)TEM.

Synthetic Vaterite Synthesis. A total of 100 mL of 50 mM $CaCl_2{\cdot}2H_2O$ was equilibrated by KOH to have a pH of 13. In parallel, 100 mL of 50 mM $NaHCO_3$ solution was prepared. Both solutions were cooled to 5 °C, after which the $CaCl_2$ solution was added to the second solution via a syringe pump at a rate of 1.5 mL/min, over 1 h with gentle stirring. The formed powder was filtered and air-dried at room temperature followed by drying in a vacuum oven at 60 °C for 2 h.

ASSOCIATED CONTENT

Supporting Information

The Supporting Information is available free of charge on the ACS Publications website at DOI: 10.1021/acs.chemmater.5b01542.

Figures S1−S9, detailed methods (PDF)

AUTHOR INFORMATION

Corresponding Author

*(P.U.P.A.G.) E-mail: pupa@physics.wisc.edu.

Notes

The authors declare no competing financial interest.

[∇](P.U.P.A.G.) Previously publishing as Gelsomina De Stasio.

ACKNOWLEDGMENTS

We thank Steve Weiner for his review of the manuscript and suggestions for improvements before submission and Lara Estroff for discussions. B.P. and P.U.P.A.G. acknowledge joint support from US-Israel Binational Science Foundation (BSF-2010065). P.U.P.A.G. acknowledges support from NSF (DMR-1105167), DOE (DE-FG02-07ER15899), and the Radcliffe Institute for Advanced Study at Harvard University. B.P. acknowledges support from the European Research Council under the European Union's Seventh Framework Program (FP/2007−2013)/ERC Grant Agreement No. [336077]. PEEM experiments were done at the ALS, supported by DOE Grant DE-AC02-05CH11231.

REFERENCES

(1) Heuer, A. H.; Fink, D. J.; Laraia, V. J.; Arias, J. L.; Calvert, P. D.; Kendall, K.; Messing, G. L.; Blackwell, J.; Rieke, P. C.; Thompson, D. H.; Wheeler, A. P.; Veis, A.; Caplan, A. I. Innovative materials processing strategies - a biomimetic approach. *Science* **1992**, *255*, 1098−1105.

(2) Gordon, L. M.; Joester, D. Nanoscale chemical tomography of buried organic-inorganic interfaces in the chiton tooth. *Nature* **2011**, *469*, 194−197.

(3) McKee, M. D.; Addison, W. N.; Kaartinen, M. T. Hierarchies of extracellular matrix and mineral organization in bone of the

DOI: 10.1021/acs.chemmater.5b01542
Chem. Mater. 2015, 27, 6516−6523

craniofacial complex and skeleton. *Cells Tissues Organs* **2005**, *181*, 176−188.
(4) Weaver, J. C.; Milliron, G. W.; Miserez, A.; Evans-Lutterodt, K.; Herrera, S.; Gallana, I.; Mershon, W. J.; Swanson, B.; Zavattieri, P.; DiMasi, E.; Kisailus, D. The stomatopod dactyl club: a formidable damage-tolerant biological hammer. *Science* **2012**, *336*, 1275−1280.
(5) Raven, J. A.; Knoll, A. H. Non-skeletal biomineralization by eukaryotes: matters of moment and gravity. *Geomicrobiol. J.* **2010**, *27*, 572−584.
(6) Siponen, M. I.; Legrand, P.; Widdrat, M.; Jones, S. R.; Zhang, W. J.; Chang, M. C. Y.; Faivre, D.; Arnoux, P.; Pignol, D. Structural insight into magnetochrome-mediated magnetite biomineralization. *Nature* **2013**, *502*, 681−684.
(7) Lowenstam, H. A.; Weiner, S. *On Biomineralization*; Oxford University Press: Oxford, 1989; p 324.
(8) Weber, E.; Pokroy, B. Intracrystalline inclusions within single crystalline hosts: from biomineralization to bio-inspired crystal growth. *CrystEngComm* **2015**, *17*, 5873−5883.
(9) Poloni, L. N.; Ward, M. D. The materials science of pathological crystals. *Chem. Mater.* **2014**, *26*, 477−495.
(10) Wesson, J. A.; Ward, M. D. Pathological biomineralization of kidney stones. *Elements* **2007**, *3*, 415−421.
(11) Dalbeck, P.; Cusack, M. Crystallography (electron backscatter diffraction) and chemistry (electron probe microanalysis) of the avian eggshell. *Cryst. Growth Des.* **2006**, *6*, 2558−2562.
(12) Cusack, M.; Dauphin, Y.; Chung, P.; Perez-Huerta, A.; Cuif, J. P. Multiscale structure of calcite fibres of the shell of the brachiopod Terebratulina retusa. *J. Struct. Biol.* **2008**, *164*, 96−100.
(13) Checa, A. G.; Esteban-Delgado, F. J.; Ramirez-Rico, J.; Rodriguez-Navarro, A. B. Crystallographic reorganization of the calcitic prismatic layer of oysters. *J. Struct. Biol.* **2009**, *167*, 261−270.
(14) Goetz, A. J.; Steinmetz, D. R.; Griesshaber, E.; Zaefferer, S.; Raabe, D.; Kelm, K.; Irsen, S.; Sehrbrock, A.; Schmahl, W. W. Interdigitating biocalcite dendrites form a 3-D jigsaw structure in brachiopod shells. *Acta Biomater.* **2011**, *7*, 2237−2243.
(15) Perez-Huerta, A.; Dauphin, Y.; Cuif, J. P.; Cusack, M. High resolution electron backscatter diffraction (EBSD) data from calcite biominerals in recent gastropod shells. *Micron* **2011**, *42*, 246−251.
(16) Checa, A. G.; Mutvei, H.; Osuna-Mascaro, A. J.; Bonarski, J. T.; Faryna, M.; Berent, K.; Pina, C. M.; Rousseau, M.; Macias-Sanchez, E. Crystallographic control on the substructure of nacre tablets. *J. Struct. Biol.* **2013**, *183*, 368−376.
(17) Goetz, A. J.; Griesshaber, E.; Abel, R.; Fehr, T.; Ruthensteiner, B.; Schmahl, W. W. Tailored order: The mesocrystalline nature of sea urchin teeth. *Acta Biomater.* **2014**, *10*, 3885−3898.
(18) Gilbert, P. U. P. A.; Metzler, R. A.; Zhou, D.; Scholl, A.; Doran, A.; Young, A.; Kunz, M.; Tamura, N.; Coppersmith, S. N. Gradual Ordering in Red Abalone Nacre. *J. Am. Chem. Soc.* **2008**, *130*, 17519−17527.
(19) Olson, I. C.; Blonsky, A. Z.; Tamura, N.; Kunz, M.; Gilbert, P. U. P. A. Crystal nucleation and near-epitaxial growth in nacre. *J. Struct. Biol.* **2013**, *184*, 454−463.
(20) Falini, G.; Fermani, S.; Reggi, M.; Njegic Dzakula, B.; Kralj, D. Evidence of structural variability among synthetic and biogenic vaterite. *Chem. Commun.* **2014**, *50*, 15370−15373.
(21) Lowenstam, H. A.; Abbott, D. P. Vaterite: a mineralization product of the hard tissues of a marine organism (Ascidiacea). *Science* **1975**, *188*, 363−365.
(22) Kamhi, S. On the structure of vaterite $CaCO_3$. *Acta Crystallogr.* **1963**, *16*, 770−772.
(23) Kabalah-Amitai, L.; Mayzel, B.; Kauffmann, Y.; Fitch, A. N.; Bloch, L.; Gilbert, P. U. P. A.; Pokroy, B. Vaterite crystals contain two interspersed crystal sructures. *Science* **2013**, *340*, 454−457.
(24) Kabalah-Amitai, L.; Mayzel, B.; Zaslansky, P.; Kauffmann, Y.; Clotens, P.; Pokroy, B. Unique crystallographic pattern in the macro to atomic structure of *Herdmania momus* vateritic spicules. *J. Struct. Biol.* **2013**, *183*, 191−198.
(25) Metzler, R. A.; Abrecht, M.; Olabisi, R. M.; Ariosa, D.; Johnson, C. J.; Frazer, B. H.; Coppersmith, S. N.; Gilbert, P. U. P. A. Architecture of columnar nacre, and implications for its formation mechanism. *Phys. Rev. Lett.* **2007**, *98*, 268102.
(26) Metzler, R. A.; Zhou, D.; Abrecht, M.; Chiou, J.-W.; Guo, J.; Ariosa, D.; Coppersmith, S. N.; Gilbert, P. U. P. A. Polarization-dependent imaging contrast in abalone shells. *Phys. Rev. B: Condens. Matter Mater. Phys.* **2008**, *77*, 064110.
(27) Gilbert, P. U. P. A.; Young, A.; Coppersmith, S. N. Measurement of c-axis angular orientation in calcite ($CaCO_3$) nanocrystals using x-ray absorption spectroscopy. *Proc. Natl. Acad. Sci. U. S. A.* **2011**, *108*, 11350−11355.
(28) DeVol, R. T.; Metzler, R. A.; Kabalah-Amitai, L.; Pokroy, B.; Politi, Y.; Gal, A.; Addadi, L.; Weiner, S.; Fernandez-Martinez, A.; Demichelis, R.; Gale, J. D.; Ihli, J.; Meldrum, F. C.; Blonsky, A. Z.; Killian, C. E.; Salling, C. B.; Young, A. T.; Marcus, M. A.; Scholl, A.; Doran, A.; Jenkins, C.; Bechtel, H. A.; Gilbert, P. U. P. A. Oxygen spectroscopy and Polarization-dependent Imaging Contrast (PIC)-mapping of calcium carbonate minerals and biominerals. *J. Phys. Chem. B* **2014**, *118*, 8449−8457.
(29) De Stasio, G.; Frazer, B. H.; Gilbert, B.; Richter, K. L.; Valley, J. W. Compensation of charging in X-PEEM: a successful test on mineral inclusions in 4.4 Ga old zircon. *Ultramicroscopy* **2003**, *98*, 57−62.
(30) Gilbert, B.; Andres, R.; Perfetti, P.; Margaritondo, G.; Rempfer, G.; De Stasio, G. Charging phenomena in PEEM imaging and spectroscopy. *Ultramicroscopy* **2000**, *83*, 129−139.
(31) Gilbert, P. U. P. A. Polarization-dependent Imaging Contrast (PIC) mapping reveals nanocrystal orientation patterns in carbonate biominerals. *J. Electron Spectrosc. Relat. Phenom.* **2012**, *185*, 395−405.
(32) Doran, A.; Church, M.; Miller, T.; Morrison, G.; Young, A. T.; Scholl, A. Cryogenic PEEM at the Advanced Light Source. *J. Electron Spectrosc. Relat. Phenom.* **2012**, *185*, 340−346.
(33) Stöhr, J.; Baberschke, K.; Jaeger, R.; Treichler, R.; Brennan, S. Orientation of chemisorbed molecules from surface-absorption fine-structure measurements: CO and NO on Ni (100). *Phys. Rev. Lett.* **1981**, *47*, 381.
(34) Olson, I. C.; Kozdon, R. H.; Valley, J. W.; Gilbert, P. U. P. A. Mollusk Shell Nacre Ultrastructure Correlates with Environmental Temperature and Pressure. *J. Am. Chem. Soc.* **2012**, *134*, 7351−7358.
(35) Checa, A. G.; Cartwright, J. H. E.; Willinger, M. G. Mineral bridges in nacre. *J. Struct. Biol.* **2011**, *176*, 330−339.
(36) Checa, A. G.; Cartwright, J. H. E.; Willinger, M.-G. The key role of the surface membrane in why gastropod nacre grows in towers. *Proc. Natl. Acad. Sci. U. S. A.* **2009**, *106*, 38−43.
(37) Van Swygenhoven, H.; Farkas, D.; Caro, A. Grain-boundary structures in polycrystalline metals at the nanoscale. *Phys. Rev. B: Condens. Matter Mater. Phys.* **2000**, *62*, 831−838.
(38) Asenath-Smith, E.; Estroff, L. A. Sectioning of Individual Hematite Pseudocubes with Focused Ion Beam Enables Quantitative Structural Characterization at Nanometer Length Scales. *Microsc. Microanal.* **2014**, *20*, 635−644.
(39) Hull, D.; Bacon, D. J. *Introduction to dislocations*; Elsevier: 2011; Vol. *37*.
(40) Shtukenberg, A. G.; Punin, Y. O.; Gunn, E.; Kahr, B. Spherulites. *Chem. Rev.* **2012**, *112*, 1805−1838.
(41) Sand, K. K.; Rodriguez-Blanco, J. D.; Makovicky, E.; Benning, L. G.; Stipp, S. L. S. Crystallization of CaCO3 in Water-Alcohol Mixtures: Spherulitic Growth, Polymorph Stabilization, and Morphology Change. *Cryst. Growth Des.* **2012**, *12*, 842−853.
(42) Gránásy, L.; Pusztai, T.; Tegze, G.; Warren, J. A.; Douglas, J. F. Growth and form of spherulites. *Phys Rev E* **2005**, *72*, 011605.
(43) Holmes, A. *The Nomenclature of Petrology*, 2nd ed.; Thomas Murby and Co.: London, 1928; p 284.
(44) Bryan, W. H. *Spherulites and allied structures. Part I*; University of Queensland Press: 1941.
(45) Yang, L.; Killian, C. E.; Kunz, M.; Tamura, N.; Gilbert, P. U. P. A. Biomineral nanoparticles are space-filling. *Nanoscale* **2011**, *3*, 603−609.
(46) Vallentyne, J. R. Isolation of pyrite spherules from recent sediments. *Limnol. Oceanogr.* **1963**, *8*, 16−29.

DOI: 10.1021/acs.chemmater.5b01542
Chem. Mater. 2015, 27, 6516−6523

(47) Wang, Q. W.; Morse, J. W. Pyrite formation under conditions approximating those in anoxic sediments 0.1. Pathway and morphology. *Mar. Chem.* **1996**, *52*, 99−121.
(48) Nindiyasari, F.; Griesshaber, E.; Fernández-Díaz, L.; Astilleros, J. M.; Sanchez-Pastor, N.; Ziegler, A.; Schmahl, W. W. Effects of Mg and Hydrogel Solid Content on the Crystallization of Calcium Carbonate in Biomimetic Counter-diffusion Systems. *Cryst. Growth Des.* **2014**, *14*, 4790−4802.
(49) Nindiyasari, F.; Ziegler, A.; Griesshaber, E.; Fernández-Díaz, L.; Huber, J.; Walther, P.; Schmahl, W. W. Effect of Hydrogel Matrices on Calcite Crystal Growth Morphology, Aggregate Formation, and Co-Orientation in Biomimetic Experiments and Biomineralization Environments. *Cryst. Growth Des.* **2015**, *15*, 2667−2685.
(50) Sivakumar, G. R.; Girija, E. K.; Kalkura, S. N.; Subramanian, C. Crystallization and characterization of calcium phosphates: Brushite and monetite. *Cryst. Res. Technol.* **1998**, *33*, 197−205.
(51) Shtukenberg, A.; Freundenthal, J.; Gunn, E.; Yu, L.; Kahr, B. Glass-crystal growth mode for testosterone propionate. *Cryst. Growth Des.* **2011**, *11*, 4458−4462.
(52) Beck, R.; Malthe-Sorenssen, D.; Andreassen, J. P. Formation and ageing of L-glutamic acid spherulites. *Cryst. Res. Technol.* **2010**, *45*, 753−762.
(53) Hoffman, J.; Frolen, L.; Ross, G.; Lauritzen, J. Growth-rate of spherulites and axialites from melt in polyethylene fractions-regime-1 and regime-2 crystallization. *J. Res. Natl. Bur. Stand., Sect. A* **1975**, *79*, 671−699.
(54) Keith, H. D.; Padden, F. J. A phenomenological theory of spherulitic crystallization. *J. Appl. Phys.* **1963**, *34*, 2409−2421.
(55) Harris, J.; Mey, I.; Hajir, M.; Mondeshki, M.; Wolf, S. E. Pseudomorphic transformation of amorphous calcium carbonate films follows spherulitic growth mechanisms and can give rise to crystal lattice tilting. *CrystEngComm* **2015**, *17*, 6831−6837.
(56) Gal, A.; Kahil, K.; Vidavsky, N.; DeVol, R. T.; Gilbert, P. U. P. A.; Fratzl, P.; Weiner, S.; Addadi, L. Particle accretion mechanism underlies biological crystal growth from an amorphous precursor phase. *Adv. Funct. Mater.* **2014**, *24*, 5420−5426.
(57) Gal, A.; Habraken, W.; Gur, D.; Fratzl, P.; Weiner, S.; Addadi, L. Calcite crystal growth by a solid-state transformation of stabilized amorphous calcium carbonate nanospheres in a hydrogel. *Angew. Chem., Int. Ed.* **2013**, *52*, 4867−4870.
(58) Dauphin, Y. Nanostructures de la nacre des tests de c6phalopodes actuels. *Paläontologische Zeitschrifl* **2001**, *75*, 113−122.
(59) Gal, A.; Weiner, S.; Addadi, L. A perspective on underlying crystal growth mechanisms in biomineralization: solution mediated growth versus nanosphere particle accretion. *CrystEngComm* **2015**, *17*, 2606−2615.
(60) De Yoreo, J. J.; Gilbert, P. U. P. A.; Sommerdijk, N. A. M. J.; Penn, R. L.; Whitelam, S.; Joester, D.; Zhang, H. Z.; Rimer, J. D.; Navrotsky, A.; Banfield, J. F.; Wallace, A. F.; Michel, F. M.; Meldrum, F. C.; Cölfen, H.; Dove, P. M. Crystallization by particle attachment in synthetic, biogenic, and geologic environments. *Science* **2015**, *349*, aaa6760.
(61) DeVol, R. T.; Sun, C.-Y.; Marcus, M. A.; Coppersmith, S. N.; Myneni, S. C. B.; Gilbert, P. U. P. A. Nanoscale transforming mineral phases in fresh nacre. *J. Am. Chem. Soc.* **2015**, (accepted for publication) DOI: 10.1021/jacs.5b07931
(62) Young, J. R.; Henriksen, K. Biomineralization within vesicles: the calcite of coccoliths. In *Biomineralization*; Mineralogical Society of America: 2003; Vol. *54*, pp 189−215.
(63) Sondi, I.; Škapin, S.; Jurina, I.; Slovenec, D. A novel concept in the growth and design of anhydrous carbonate minerals: nano-scale aggregation mechanisms. *Geol. Croat.* **2011**, *64*, 61−65.
(64) Sone, E. D.; Weiner, S.; Addadi, L. Morphology of Goethite Crystals in Developing Limpet Teeth: Assessing Biological Control over Mineral Formation. *Cryst. Growth Des.* **2005**, *5*, 2131−2138.
(65) Beniash, E.; Metzler, R. A.; Lam, R. S. K.; Gilbert, P. U. P. A. Transient amorphous calcium phosphate in forming enamel. *J. Struct. Biol.* **2009**, *166*, 133−143.
(66) Simmer, J. P.; Hu, J. C. C. Expression, structure, and function of enamel proteinases. *Connect. Tissue Res.* **2002**, *43*, 441−449.
(67) Nielsen, M. H.; Aloni, S.; De Yoreo, J. J. In situ TEM imaging of $CaCO_3$ nucleation reveals coexistence of direct and indirect pathways. *Science* **2014**, *345*, 1158−1162.
(68) Andreassen, J. P. Formation mechanism and morphology in precipitation of vaterite - nano aggregation or crystal growth? *J. Cryst. Growth* **2005**, *274*, 256−264.
(69) Addadi, L.; Weiner, S. Interactions between acidic proteins and crystals: stereochemical requirements in biomineralization. *Proc. Natl. Acad. Sci. U. S. A.* **1985**, *82*, 4110−4114.
(70) Metzler, R. A.; Evans, J. S.; Killian, C. E.; Zhou, D.; Churchill, T. H.; Appathurai, N. P.; Coppersmith, S. N.; Gilbert, P. U. P. A. Nacre protein fragment templates lamellar aragonite growth. *J. Am. Chem. Soc.* **2010**, *132*, 6329−6334.
(71) Bryan, W. H.; Hill, D. *Spherulitic crystallization as a mechanism of skeletal growth in the hexacorals*; Proceedings of the Royal Society of Queensland LII, 79−91 (1941).
(72) Falini, G.; Fermani, S.; Vanzo, S.; Miletic, M.; Zaffino, G. Influence on the formation of aragonite or vaterite by otolith macromolecules. *Eur. J. Inorg. Chem.* **2005**, *2005*, 162−167.
(73) Wittmann, K.; Schlacher, T.; Ariani, A. Structure of Recent and fossil mysid statoliths (Crustacea, Mysidacea). *J. Morphol.* **1993**, *215*, 31−49.
(74) Wright, C. G.; Rouse, R. C.; Zajic, G. H.; Schaefer, S. D.; Hubbard, D. G.; Barnard, L. A. A calcareous concretion in the posterior semicircular duct of a human labyrinth. *Am. J. Otolaryngol.* **1982**, *3*, 196−201.
(75) Gauldie, R. Polymorphic crystalline structure of fish otoliths. *J. Morphol.* **1993**, *218*, 1−28.
(76) Nys, Y.; Hincke, M.; Arias, J.; Garcia-Ruiz, J.; Solomon, S. Avian eggshell mineralization. *Poultry Avian Biol. Rev.* **1999**, *10*, 143−166.
(77) Vianey-Liaud, M.; Hirsch, K.; Sahni, A.; Sige, B. Late Cretaceous Peruvian eggshells and their relationships with Laurasian and Eastern Gondwanian material. *Geobios* **1997**, *30*, 75−90.
(78) Benzerara, K.; Menguy, N.; Obst, M.; Stolarski, J.; Mazur, M.; Tylisczak, T.; Brown, G. E., Jr; Meibom, A. Study of the crystallographic architecture of corals at the nanoscale by scanning transmission X-ray microscopy and transmission electron microscopy. *Ultramicroscopy* **2011**, *111*, 1268−1275.
(79) Cuif, J. P.; Dauphin, Y. The two-step mode of growth in the Scleractinian coral skeletons from the micrometre to the overall scale. *J. Struct. Biol.* **2005**, *150*, 319−331.
(80) Rodriguez-Navarro, A.; Jimenez-Lopez, C.; Hernandez-Hernandez, A.; Checa, A.; Garcia-Ruiz, J. M. Nanocrystalline structures in calcium carbonate biominerals. *J. Nanophotonics* **2008**, *2*, 021935.
(81) Achilles, W.; Jockel, U.; Schaper, A.; Burk, M.; Riedmiller, H. In-vitro formation of urinary stones - generation of spherulites of calcium-phosphate in gel and overgrowth with calcium-oxalate using a new flow model of crystallization. *Scanning Microsc.* **1995**, *9*, 577−586.
(82) Sokol, E.; Nigmatulina, E.; Maksimova, N.; Chiglintsev, A. CaC_2O_4-H_2O spherulites in human kidney stones: morphology, chemical composition, and growth regime. *Eur. J. Mineral.* **2005**, *17*, 285−295.
(83) Al-Atar, U.; Bokov, A. A.; Marshall, D.; Teichman, J. M. H.; Gates, B. D.; Ye, Z.-G.; Branda, N. R. Mechanism of calcium oxalate monohydrate kidney stones formation: layered spherulitic growth. *Chem. Mater.* **2010**, *22*, 1318−1329.
(84) Khan, S. R.; Hackett, R. L. Role of organic matrix in urinary stone formation - an ultrastructural-study of crystal matrix interface of calcium-oxalate monohydrate stones. *J. Urol.* **1993**, *150*, 239−245.
(85) Andreassen, J.-P.; Beck, R.; Nergaard, M. Biomimetic type morphologies of calcium carbonate grown in absence of additives. *Faraday Discuss.* **2012**, *159*, 247−261.
(86) Frenzel, M.; Harper, E. M. Micro-structure and chemical composition of vateritic deformities occurring in the bivalve Corbicula fluminea (Müller, 1774). *J. Struct. Biol.* **2011**, *174*, 321−332.

DOI: 10.1021/acs.chemmater.5b01542
Chem. Mater. 2015, 27, 6516−6523

(87) Frenzel, M.; Harrison, R. J.; Harper, E. M. Nanostructure and crystallography of aberrant columnar vaterite in Corbicula fluminea (Mollusca). *J. Struct. Biol.* **2012**, *178*, 8−18.
(88) Isaure, M.-P.; Sarret, G.; Harada, E.; Choi, Y.-E.; Marcus, M. A.; Fakra, S. C.; Geoffroy, N.; Pairis, S.; Susini, J.; Clemens, S.; Manceau, A. Calcium promotes cadmium elimination as vaterite grains by tobacco trichomes. *Geochim. Cosmochim. Acta* **2010**, *74*, 5817−5834.
(89) Qiao, L.; Feng, Q.-L.; Li, Z. Special vaterite found in freshwater lackluster pearls. *Cryst. Growth Des.* **2007**, *7*, 275−279.
(90) Lakshminarayanan, R.; Chi-Jin, E. O.; Loh, X. J.; Kini, R. M.; Valiyaveettil, S. Purification and characterization of a vaterite-inducing peptide, pelovaterin, from the eggshells of Pelodiscus sinensis (Chinese soft-shelled turtle). *Biomacromolecules* **2005**, *6*, 1429−1437.
(91) Wehrmeister, U.; Soldati, A. L.; Jacob, D. E.; Häger, T.; Hofmeister, W. Raman spectroscopy of synthetic, geological and biological vaterite: a Raman spectroscopic study. *J. Raman Spectrosc.* **2010**, *41*, 193−201.

DOI: 10.1021/acs.chemmater.5b01542
Chem. Mater. 2015, 27, 6516−6523

Supporting Information:
Figures S1-S9, Detailed Methods

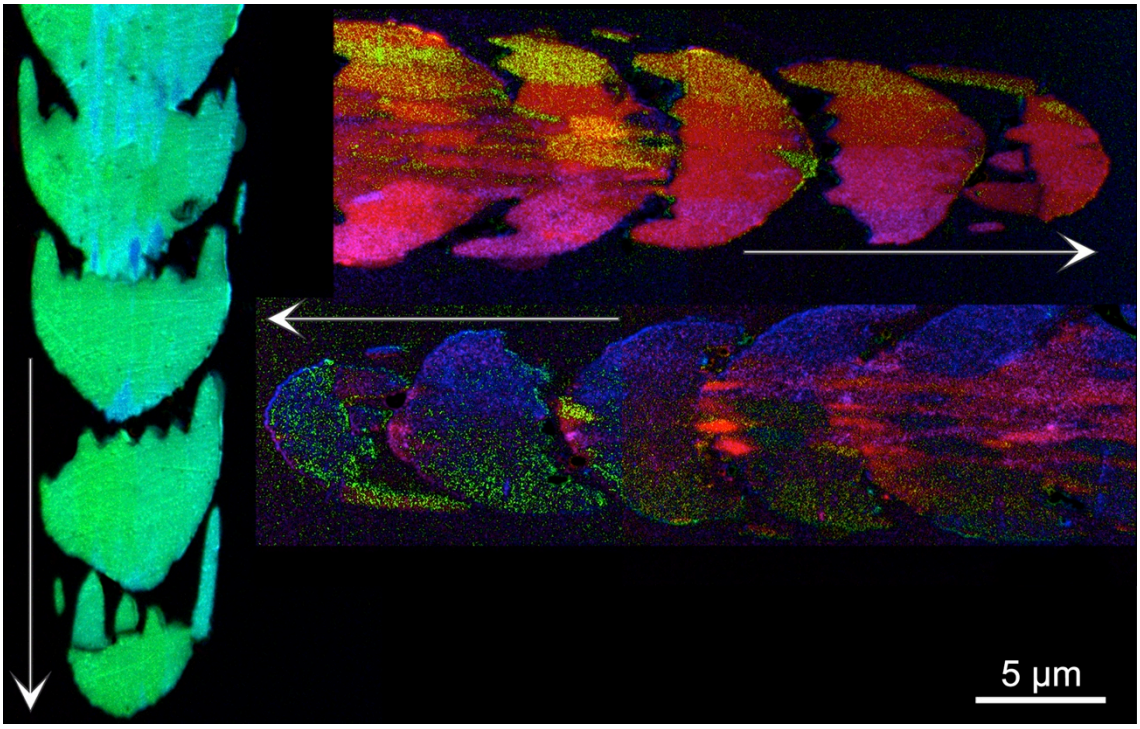

Figure S1. PIC-maps of the same spicule in 3 positions. All 3 images are identical to those in Figure 2 in size and position, but all 3 here have been brightness-enhanced by adjusting "levels" in Adobe Photoshop®. This enhancement makes it possible to see both horizontal spicules, and may be more aesthetically pleasing, but the color and brightness are no longer representative, nor quantitative.

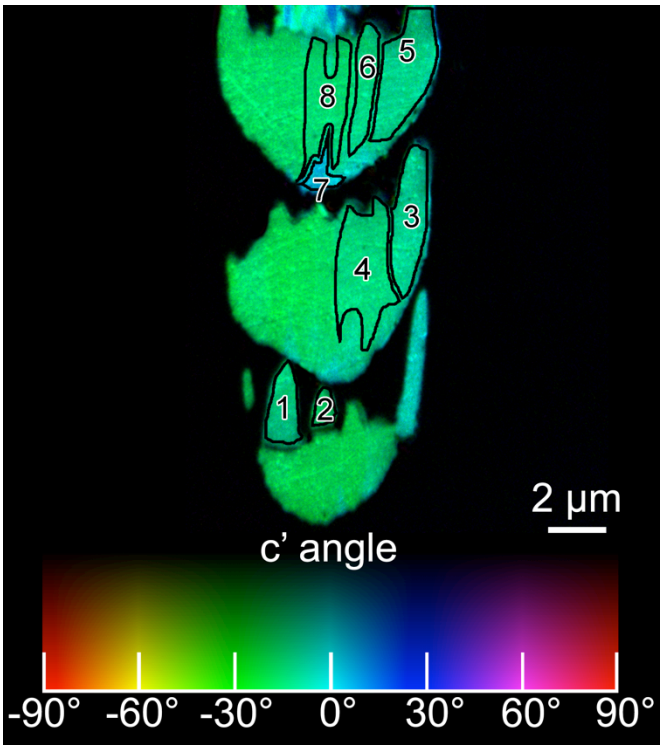

Figure S2. Spicule T1 in Figures 1 and 2, showing regions 1-8, from which the orientation data for Table 1 were extracted.

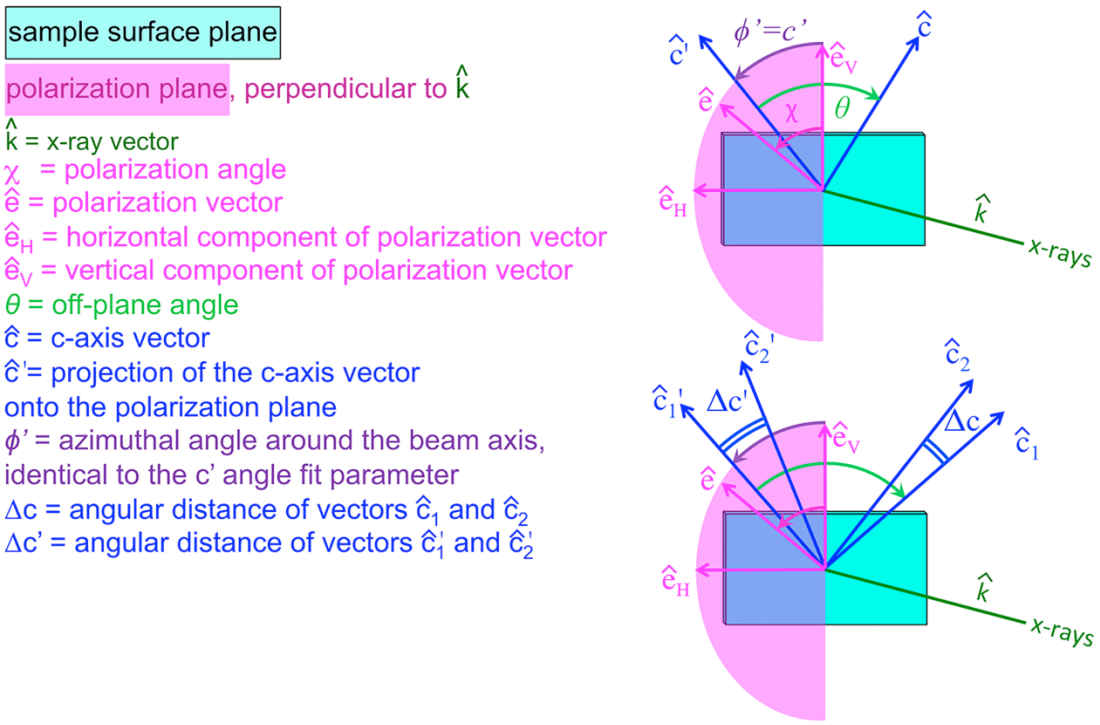

Figure S3. Schematic showing (top) other relevant angles used in section 4 of the methods, (bottom) the angular distances □*c* and □*c*' measured in Table 1 and for the data of Figure 3.

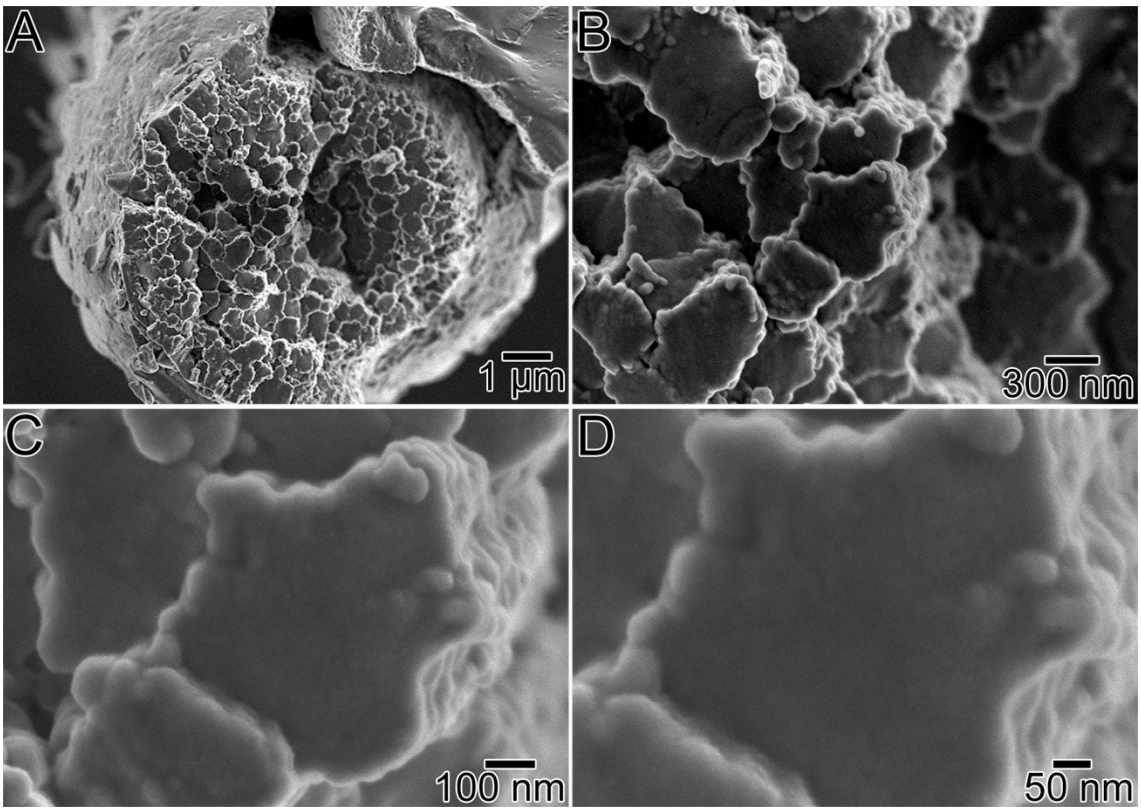

Figure S4. Increasing magnification SEM micrographs of a body spicule cryo-fractured in liquid nitrogen. Notice that at the highest magnification no nanoparticulate texture appears in a broken core crystallite.

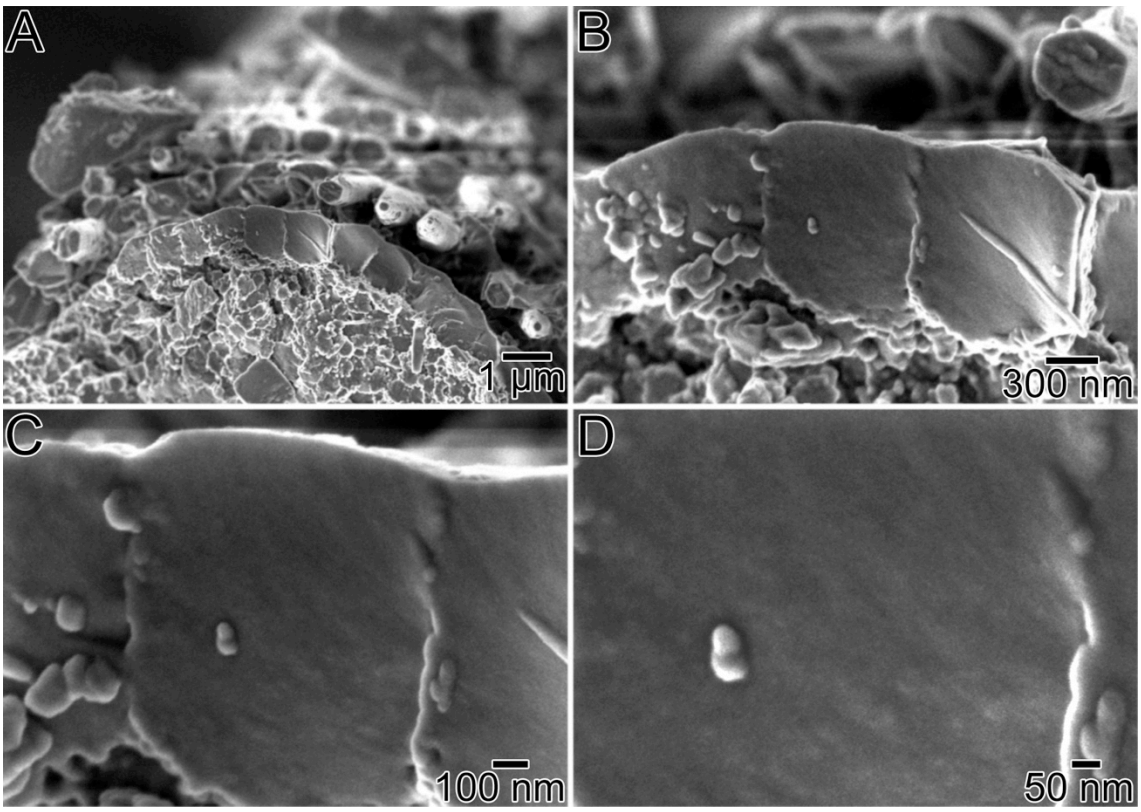

Figure S5. SEM micrographs of another cryo-fractured body spicule. Again, no nanoparticulate texture appears in broken thorns even at the highest magnifications. Notice the hexagonal cross-section of euhedral crystal on top right of B.

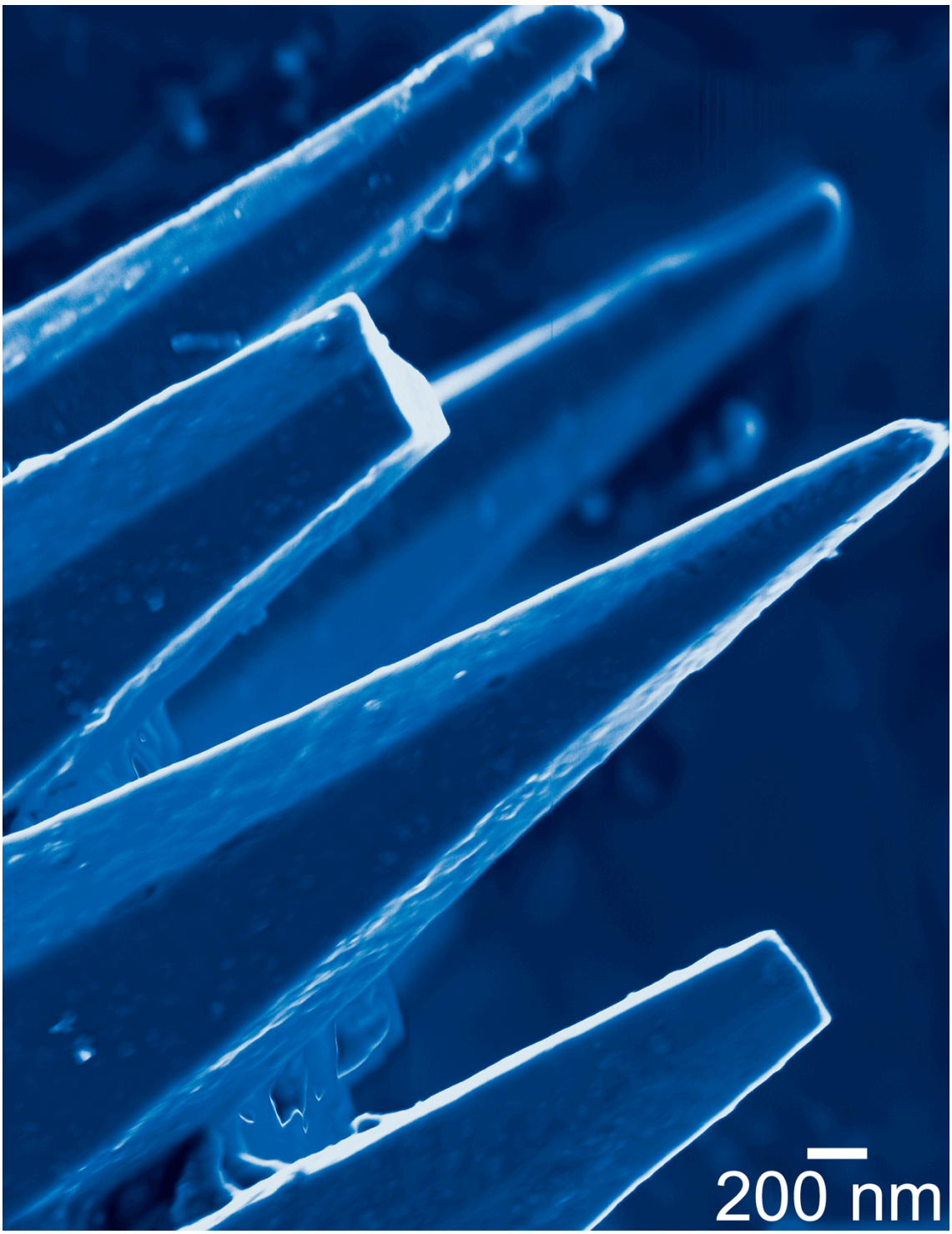

Figure S6. SEM micrograph of euhedral thorn crystals. Two thorns show smooth, non-nanoparticulate fracture (albeit overexposed), the other three are complete hexagonal pyramidal crystals. The original grayscale images was converted to a tri-tone image in Adobe Photoshop, using linear white, non-linear black and blue profiles, which were custom-designed.

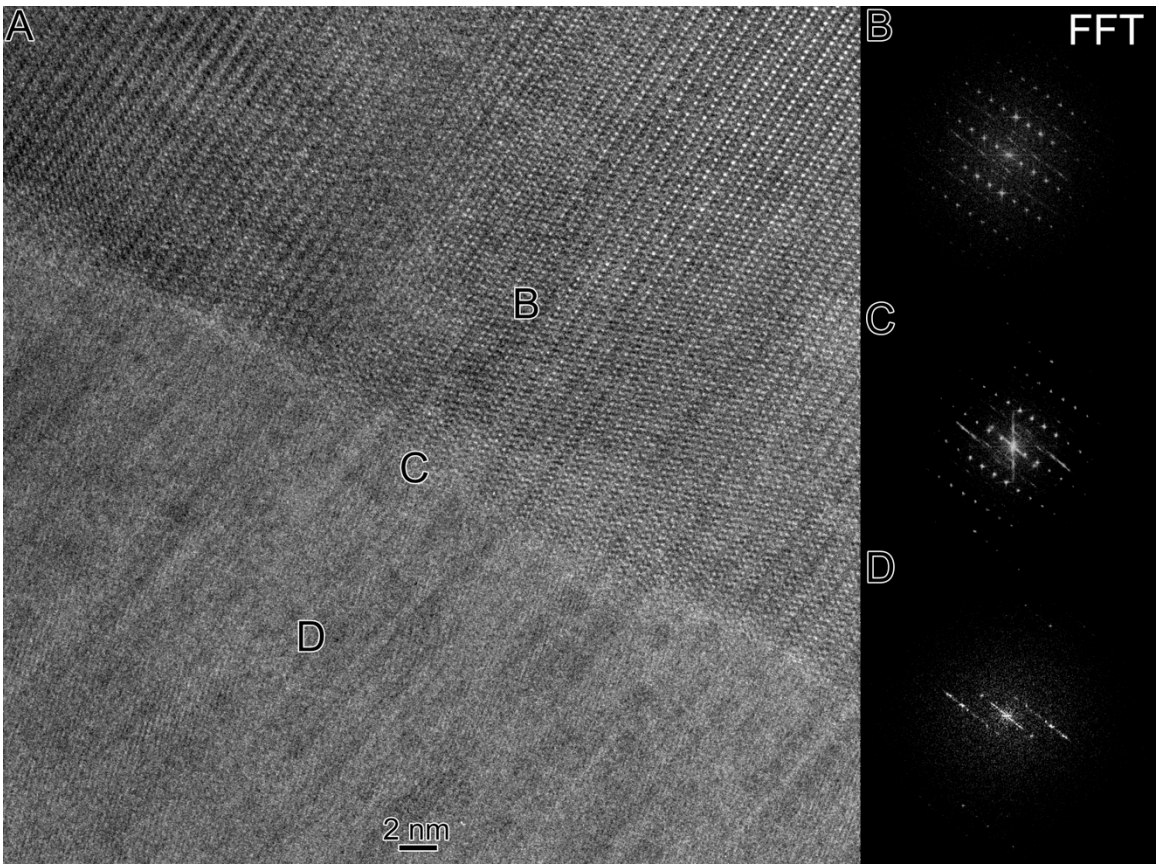

Figure S7. (A) HRTEM micrograph of a portion of body spicule, including a core and a thorn crystal. B, C, D. Fast Fourier Transform (FFT) of the image obtained from the (B) core crystal region, (C) the interface, and (D) the thorn crystal region. Even though the core crystal is in better focus than the thorn crystal, it is clear that the two crystal lattices abut one another with no organics or voids at their interface. The interface clearly shows the FFT pattern from both crystal lattices.

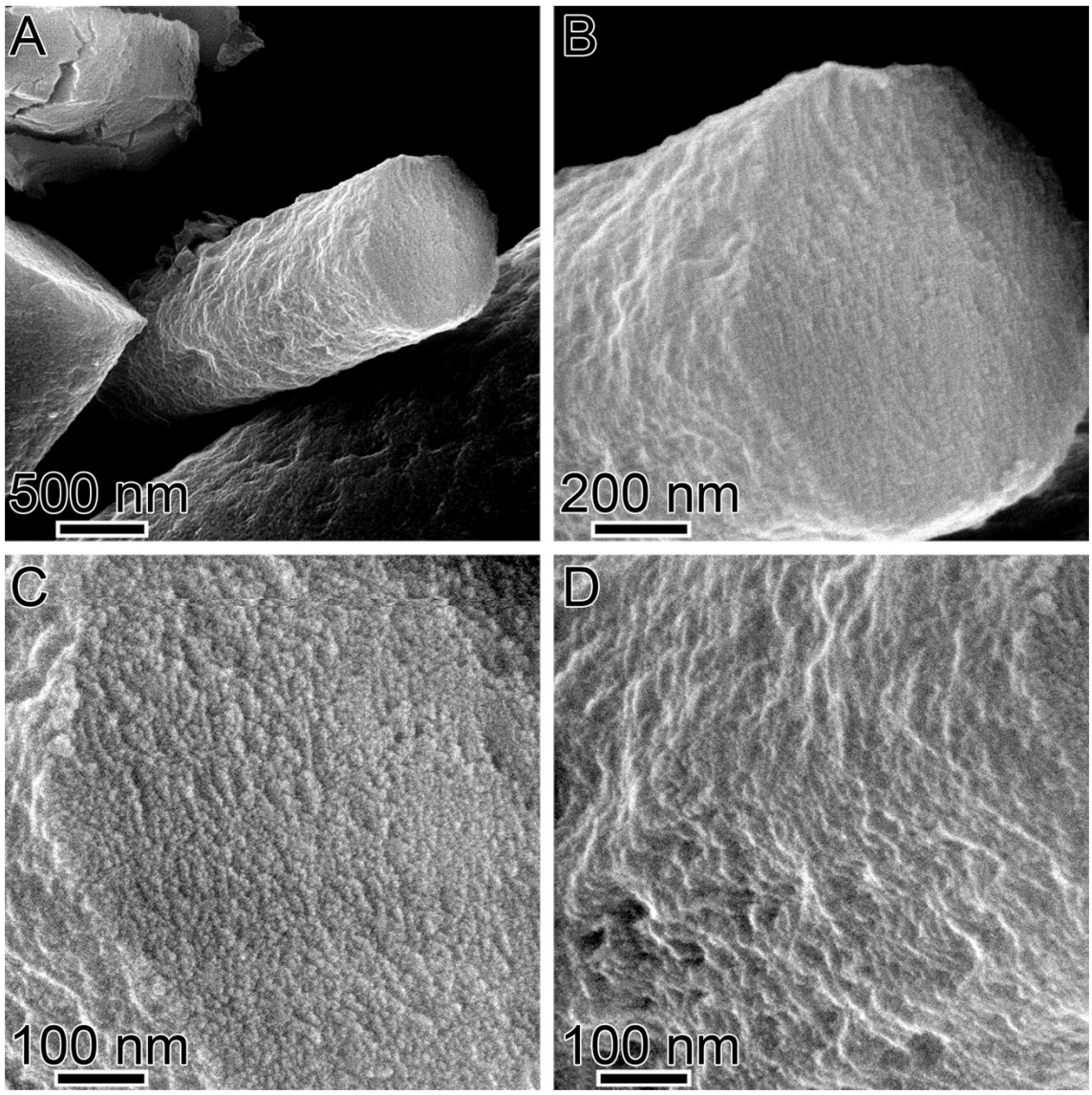

Figure S8. SEM micrographs of sea urchin spicules cryo-fractured in LN_2, at increasing magnifications. Notice the nanoparticulate texture in the spicule cross-section (C) and on the cylindrical side surface (D).

Detailed Methods

1. Sample preparation and PEEM data acquisition

Herdmania momus spicules were extracted as described in [1, 2], synthetic vaterite was prepared as follows: 50 ml of 20 mM sodium carbonate solution was added stepwise over 10 min to 50 ml of 20 mM $CaCl_2$ solution while stirring. All solutions were first cooled to 5°C prior to reaction and Ammonium hydroxide was added prior to reaction to the $CaCl_2$ solution so that the starting pH was 11. After all the sodium carbonate solution was added to the calcium chloride solution the mixture was allowed to rest for 5 min, then filtered and the powder collected was dried in a vacuum oven over night at 120°C.

Spicules were double-rinsed in ethanol, embedded in EpoFix (EMS, Hatfiled, PA), along with synthetic vaterite in the same EpoFix blocks, polished with 300nm, then 50nm Al_2O_3 suspension (MicroPolish and MasterPrep, respectively, Buehler, Lake Bluff, IL) dialyzed against 22 g/L Na_2CO_3 in DDH_2O [3]. The polished sample was rinsed in Na_2CO_3 solution, then ethanol, air-dried, and finally coated with 1 nm Pt in the area to be analyzed by PEEM, and 40 nm Pt around it, as described in [3-5]. They were then analyzed in PEEM-3 at the Advanced Light Source (ALS) [6]. We acquired images at x-ray polarizations varying in increments of 5° from horizontal to vertical (19 images), while maintaining the photon energy constant at 534 eV, at the most polarization-sensitive oxygen K-edge π* peak. The rotator used to acquire the images in Figures 2 and S1 is transferred in and out of the vacuum chamber along with the sample. This device rotates the sample position azimuthally, that is, around the normal to the sample surface. We imaged the end of the spicule (T1 in Figure 1) opposite to the tip we wished to image for Figure 2, rotated the sample by ~10° at a time, and placed the end of the spicule back into the field of view. Once each 90° rotation was complete, we moved to the tip of the spicule, re-adjusted tilt, focus, and stigmators, and acquired a new stack of 19 images.

For all images the field of view was 20 μm, and the pixel size 20 nm. The sample voltage was -18 kV, and the microscope pressure $1\square10^{-8}$ Torr. All data processing to produce the color PIC-maps was done in Igor Pro® (WaveMetrics, Lake Oswego, OR), using Gilbert Group (GG) Macros, distributed free of charge on our web site [7].

2. Color PIC-mapping

In GG Macros [7] the intensity vs. polarization angle curve from each pixel was fit to the equation $f(\chi) = a + b\cos^2(\chi - c')$, where a, b, c' are fit parameters.

Each polarization-dependent intensity curve is normalized to the beamline Izero before the fit is performed, so a and b are dimensionless quantities; c' is and angle in degrees.

For calcite and aragonite the maximum x-ray linear dichroism, that is, the maximum response to polarized light, occurs when the polarization is parallel to the *c*-axis, and the minimum response occurs when they are perpendicular. For vaterite the opposite effect is observed: the response is maximum and minimum when the polarization is perpendicular and parallel to the *c*-axis, respectively [8]. For this reason, for the vaterite spicules in this work the fit parameters were transformed (in the Igor macros) in the following way:

$$a \rightarrow a + b$$
$$b \rightarrow -b$$
$$c' \rightarrow c' \pm 90°$$

where the sign in the last transformation is chosen so that $-90° \leq c' \leq +90°$. These transformations ensure that b is negative without affecting the shape of the fit curve; b must be negative for vaterite for the reason explained above. Thus **vertical** *c*-axes for calcite, aragonite, and vaterite look the same, and are displayed in **cyan**.
The hue of the PIC-map displays the *c'* angle, that is, the projection of the *c*-axis onto the polarization plane. The brightness displays the value *b*, which represents the off-plane angle of the *c*-axis (where *a*, *b*, *c'*, are the transformed values). In-plane *c*-axis is assigned maximum brightness, normal is black.
B is the largest-modulus (absolute value) for b observed in either synthetic or biogenic vaterite at hundreds of different orientations, when acquiring data with the same parameter. In the present case the parameters were: exposure time = 3 sec; exit slit 200μm horizontal 150 μm vertical; $B = -260$. Thus, maximum brightness is defined to occur for $b = B = -260$, and is identical for all vaterite PIC-maps presented here. Minimum brightness is defined to occur for $b = 0$.

Once the color PIC-map is produced by the GG Macros, the color file is exported and saved with all the relevant parameters in the filename.

For each PIC-map file we:
Opened it in Adobe Photoshop®
Placed all the vaterite images into 1 Photoshop file, each on its own layer
Rasterized all the layers to make them editable
Duplicated these layers and left the originals unedited
Hid all layers except the one at the top part of the spicule (image 1)
Cut out the colorbar at the bottom of 1, and the leftmost column of pixels, which contains artifacts.
Repeated for all layers

Placed the first 2 images at top, and flipped between 1 and 2 to check how well they match for a coarse positioning
Repeated for all layers for coarse positioning
Used perspective tool on image 2 to make it as similar as possible to 1 (edit->transform->perspective/skew)
    perspective only had to change on left side of the image
    skew used for small changes to better stitch spicules
These changes were necessary because the PEEM images have distortions at their edges.
Repeated this matching for each layer by only using the perspective and skew tool and shifting the image
Added scale bar (FOV was 20μm, so a 5 μm scalebar is 256 pixels wide) and color bar (default colors and angles, but now changed to show *c*' angle rather than π' angle as in [8], because π' angle is not well-defined for vaterite.)

3. Image Cleaning

Since the spicules are long and thin, images of partly overlapping segments were acquired for each spicule, and these needed to be stitched together. In addition, synthetic vaterite particles were embedded with the vaterite spicules, and were analyzed simultaneously; we needed to display them separately. Lastly, small distortions occur at the edges of these non-aberration corrected images, hence small adjustments termed "cleaning" were needed to seamlessly stitch them. Figure S9 shows typical images before and after image cleaning. Note that all measurements were done on the original data and not on the cleaned images.

1. We created a separate layer for cleaning. All cleaning changes are on this layer and not on the original spicule data layers, so the original data remain always retrievable, and directly comparable with the cleaned versions.
2. Outlined spicule roughly using the pencil tool.
3. Zoomed in closely and using the brush tool outline the spicule carefully (brush size varies between 5 and 70 pixels, depending on area). We erred on the side of caution and left more epoxy versus possibly shaving parts of the spicule.
4. Once the entire spicule was outlined, we filled the outside of the outline (bucket tool, no anti-aliasing, "cleaned" layer only, tolerance 1, contiguous).
5. The spicule was cleaned at this point and none of the spicule was covered since the outlining process avoided the spicule.
6. A few missing corners needed to be filled in, to do this the clone stamp tool in Adobe Photoshop® was used, hardness 3%, size variable between 10 and 100 pixels depending on the area. The edges of the clone stamp tool are blurry by default. In some cases

the edges between images differed slightly in brightness or physical dimensions due to distortions (e.g. Figure S9). We blended these few edges using the clone stamp, always only in the "cleaned" layer, so the original data are unaltered and can be retrieved if needed.

All spicules were finally combined into one file for Figure 1. For printing and display purposes, since most spicules in Figure 1 printed extremely dark, we slightly enhanced the "levels" in Photoshop® for all colored elements simultaneously, including all spicules, synthetic vaterite, and the color bar. Levels were only adjusted for Figure 1, not for Figure 2.

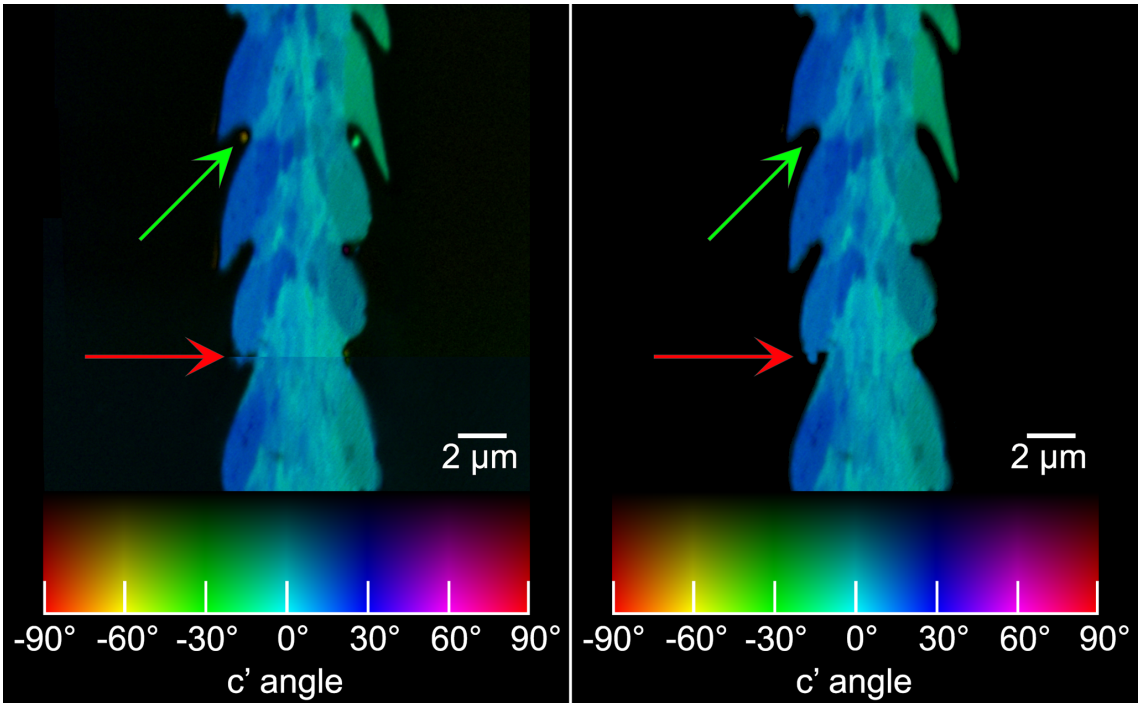

Figure S9. PIC-maps of spicule T6 before (left) and after (right) "image cleaning" as described in section 3. The green arrow points to one of the synthetic vaterite particles, clearly separate from the spicule, the red arrow shows distortion of the image on top that makes it imperfectly overlap the image below. Notice that the epoxy, which is non-polarization dependent, is completely black before and after image cleaning.

4. PIC theory in the uniaxial approximation

4.1. Definition

This section of the SI is about how to translate from PIC stacks to images and angular distances. In this, we will assume that the crystal is effectively uniaxial, so that the only direction of importance is that of an energy-independent optic axis, which would be the *c*-axis of calcite, aragonite, or vaterite.

4.2. Basics

The main assumption is that if the x-rays come in with a polarization vector $\hat{e}$ and the axis of the crystal at the pixel of interest is $\hat{c}$, then the intensity from that pixel is given by

$$I = I_0(A + B(\hat{e}\cdot\hat{c})^2) \tag{1}$$

where *A* and *B* are energy-dependent quantities [9]. Here and in what follows, unit vectors are indicated as hatted variables. Now, in PEEM-3 at the ALS, the incident beam comes in from a direction $\hat{k}$ tilted by 30° from the *x*-axis:

$$\hat{k} = (\cos\psi, 0, \sin\psi) \tag{2}$$

where the coordinate system is such that *x* is along the projection of the beam direction onto the sample surface, *z* is perpendicular to the sample, so *y* is vertical, in the plane of the sample surface and perpendicular to the beam, and the angle ψ between *x* and $\hat{k}$ is 30°. The horizontal (H) and vertical (V) polarization vectors are perpendicular to $\hat{k}$, so they must be

$$\begin{aligned}\hat{e}_H &= (\sin\psi, 0, -\cos\psi)\\ \hat{e}_V &= (0,1,0)\end{aligned} \tag{3}$$

making the polarization vector at an angle χ

$$\hat{e} = \cos\chi\hat{e}_V + \sin\chi\hat{e}_H = (\sin\chi\sin\psi, \cos\chi, -\sin\chi\cos\psi). \tag{4}$$

At χ=0°, $\hat{e}$ = (0,1,0), i.e. the polarization is vertical, along the *y* direction. At χ=90°, $\hat{e} = (\sin\psi, 0, -\cos\psi)$, and this is the most nearly perpendicular to the sample surface, in fact 30° from perpendicular.

Next, we need the *c*-axis direction in polar coordinates. We could take the polar angle as θ and the azimuthal angle as ϕ, so that the direction is

$$\hat{c} = (\cos\phi\cos\theta, \sin\phi\cos\theta, \sin\theta), \tag{5}$$

where we've taken the somewhat unusual convention that $\theta = 0$ represents the vector lying down and $\theta = 90°$ as pointing straight up. However, it will be much simpler to do the math if we take polar coordinates defined relative to the beam axis:

$$\hat{c} = \cos\theta'(\sin\phi'\hat{e}_H + \cos\phi'\hat{e}_V) + \sin\theta'\hat{k} \tag{6}$$

where ϕ' is the azimuthal angle around the beam axis (which is identical to *c*' defined above) and θ' is the polar angle, defined so that $\theta' = 90°$ means that $\hat{c}$ is along the beam axis. This we later express in terms of the sample-based polar coordinates θ, ϕ.

4.3. PIC signal

Substituting (4) and (5) into (1) yields

$$I/I_0 = A + B\cos^2\theta'\cos^2(\phi' - \chi). \tag{7}$$

The PIC-map produces a set of coefficients such that

$$I_{\mathrm{PIC}} = a + b\cos^2(\chi - c') \tag{8}$$

which leads to the identification

$$\phi' = c'$$
$$\theta' = \cos^{-1}\left(\pm\sqrt{(b/a)/(B/A)}\right). \tag{9}$$

Since θ' is a polar angle, it's restricted to the range $[0,\pi]$, which makes taking the inverse cosine unambiguous. How can we know *A* and *B*, or, more precisely, their ratio $D = B/A$? One way we could do it would be to measure a large set of random grains and look for the maximum dichroism, that is, the maximum dependence on χ. Intuitively, one would expect this to occur when the orientation is in the plane defined by the polarization vectors, i.e. perpendicular to the beam direction $\hat{k}$. Thus, one such maximum is when $\phi' = \pi/2,\ \theta' = 0$. In that case,

$$I_{\mathrm{max\_dich}} = A + B\cos^2\chi \tag{10}$$

so the ratio *B/A* may be measured as

$$D = B/A = \max\left[\frac{I_{\chi=0}}{I_{\chi=90^\circ}}\right] - 1 \tag{11}$$

where the maximum is over all crystal grains.

We note that there is an ambiguity in the measurement of the orientation of $\hat{c}$. If this unit vector is "reflected" to a position mirror-symmetric with respect to the polarization plane, so that the projection along the beam axis changes sign but the component in the plane does not, then all measured quantities remain the same. Thus, there are two possible values of orientation, which will take the same color in a PIC-map presented in terms of ϕ', θ' (hue and brightness in the main text). One way to resolve this ambiguity is to rotate the sample azimuthally, that is, around the normal to its surface; this was done for one spicule (Figure 2).

4.4. Angular distance Δc

One way to go beyond qualitative imaging and get more-quantitative data about orientation is to measure the angular distance between the orientations of adjacent grains. This measure is independent of the coordinate system used to describe the orientation. One could then compare the distribution of angular distances between adjacent grains with those of pairs of randomly-chosen grains, in order to see if adjacent grains tend to be oriented in the same direction. If we have two orientations with axes $\hat{c}_1, \hat{c}_2$, then the angular distance between them is given by

$$\Delta c = \cos^{-1}(\hat{c}_1 \cdot \hat{c}_2), \tag{12}$$

which can be evaluated using the form (6)

$$\Delta c = \cos^{-1}\left[\cos\theta_1'\cos\theta_2'\cos(\phi_1'-\phi_2') + \sin\theta_1'\sin\theta_2'\right]. \tag{13}$$

Substituting (9) into (13) yields

$$\cos\Delta c = \frac{1}{D}\left(\sqrt{\frac{b_1 b_2}{a_1 a_2}}\cos(c_1'-c_2') + \sqrt{\left(D-\frac{b_1}{a_1}\right)\left(D-\frac{b_2}{a_2}\right)}\right) \tag{14}$$

where $a_1, b_1, c_1', a_2, b_2, c_2'$ are the fit coefficients for the two grains.

A word about signs: we have implicitly assumed D to be positive, as it is for aragonite and calcite. However, vaterite has its □ orbitals in the basal plane, normal to the *c*-axis, which makes D negative. In that case, the fitting must be done so that the b coefficients are also negative, which is enforced by the correct choice of *c'*. Note that in (8), the sign of b flips if 90° is added to *c'*. Similarly, if D>0, then *c'* must be chosen so that b>0. For the Δc measurements in Table 1, D = -0.6 is used, since this is the largest-modulus d value observed in this spicule, in 3 different positions, across 6 PIC-stacks.

Further, there is the ambiguity mentioned in the previous section. If one takes two orientations and "reflects" one to a position mirror-symmetric with respect to the polarization plane, then the angular distances measured in these two positions are different. Reflecting also the second orientation brings the distance back to the original value. Thus, there are actually two possible values for the angular distance computed for any two grains. We resolve this ambiguity in Table 1 by measuring the same pairs of crystals in two different orientations, computing both possible values of Δc in both orientations, and adopting the Δc values that agree in both orientations.

4.5. Sample-centered coordinates

Transformation to these coordinates was not used for any of the data presented here. However, we include it for completeness. Suppose we now want the orientation of the axis in coordinates referred to the sample, rather than the beam, i.e. expressed as in Eq. (5) instead of (6). This is easily accomplished by taking appropriate dot products:

$$\begin{aligned}\sin\theta = \hat{c}\cdot\hat{z} &= \cos\theta'\sin\phi'\hat{e}_H\cdot\hat{z} + \cos\theta'\cos\phi'\hat{e}_V\cdot\hat{z} + \sin\theta'\hat{k}\cdot\hat{z} \\ &= -\cos\theta'\cos\phi'\cos\psi + \sin\theta'\sin\psi\end{aligned} \tag{15}$$

for the polar angle, and

$$\begin{aligned}\tan\phi = \frac{\hat{c}\cdot\hat{y}}{\hat{c}\cdot\hat{x}} &= \frac{\cos\theta'(\hat{e}_H\cdot\hat{y}\sin\phi' + \hat{e}_V\cdot\hat{y}\cos\phi') + \hat{k}\cdot\hat{y}\sin\theta'}{\cos\theta'(\hat{e}_H\cdot\hat{x}\sin\phi' + \hat{e}_V\cdot\hat{x}\cos\phi') + \hat{k}\cdot\hat{x}\sin\theta'} \\ &= \frac{\cos\theta'\sin\phi'}{\cos\theta'\sin\phi'\sin\psi + \sin\theta'\cos\psi}\end{aligned} \tag{16}$$

where caution must be used in taking the arctangent to be sure of getting in the correct quadrant. This can be done using the two-argument `atan2(y,x)` function found in many programming languages. Once this transformation is done, one can rotate an image by an angle δ and compensate by subtracting δ from ϕ. Such a procedure would, with no loss in information, let one make images of similar structures so that they're aligned the same way with consistent color schemes, even though the original images had them pointed in different directions.

4.6. Angular distance □ *c'*

We measured 100 angular distances each in biogenic and synthetic vaterite, then displayed them in 45-bin histograms (2° bins) in Figure 3.

The difference in orientation between two adjacent crystals is

$$\Delta c' = \begin{cases} 180 - \left| c_1' - c_2' \right| & \text{if} \left| c_1' - c_2' \right| > 90 \\ \left| c_1' - c_2' \right| & \text{otherwise} \end{cases} \qquad (17)$$

where c_1' and c_2' are the c' angles of two adjacent crystals 1 and 2.

To obtain the angles c_1' and c_2', crystal interfaces were found manually (5-10 per PIC map). The whole crystal is selected as a region of interest (ROI) by manually tracing its contour in Igor. The spectra in the pixels in the ROI are then averaged together, and the resulting spectrum is fit to the equation $f(\chi) = a + b\cos^2(\chi - c')$ (this is done by pressing the "*Analyze ROI as 1*" button in GG Macros, Polarization Analysis Package [7]). The value c' obtained from this fit was then transformed to be appropriate for vaterite, $c' \rightarrow c' \pm 90°$, as described above. The analysis is completed in two adjacent crystals, and the obtained values c_1' and c_2' are plugged into the equation for $\Delta c'$ above using Microsoft Excel® in order to calculate the angular distance between the two crystals.

5. SEM and TEM experiments

Most of the SEM experiments were done at the Technion Electron Microscopy Center of the Department of materials science and engineering. Figures 4, S2, S3 were acquired on a Zeiss Ultra-Plus Field Emission Gun (FEG)-SEM and an In-Lens detector, at an acceleration voltage of 1.8 kV. The images in Figures S4 and S5 were acquired at an acceleration voltage of 2.0 and 4 kV respectively.

The sea urchin spicule images in Figure S5 were acquired at the UC-Berkeley Electron Microscopy Laboratory (EML), using a Hitachi S5000 FESEM, secondary electrons, and 5.0 kV. For these experiments,

spicules were extracted from 72h embryos as described in [10], and bleached. The extracted spicules were let crystallize for about a week at room temperature, then were crushed gently in mortar and pestle, with liquid nitrogen, then were coated at EML with 1nm of Au+Pd mixture, 50%+50%.

TEM investigation was carried out at the Technion, utilizing a Titan FEI (S)TEM with a dedicated platform for corrector and monochromator technologies, which enable a resolution of 0.7 Angstrom. In order to acquire Figure 5, the sample was prepared by a FEI Strata 400S FIB. The acceleration voltage was 300 keV for imaging, whereas for diffraction we used a linescan with a beam size of 3 nm.
FIB was used for TEM sample preparation for several reasons. First, FIB enables the preparation of specific sample size by cutting a particular part of the examined object in the required direction. Second, sample preparation, utilizing microtomy, does not provide the required result due to weak adhesion between vaterite and the epoxy commonly used for microtomy. The FIB used was a Strata 400 STEM Dual-Beam system, which is a fully digital field emission scanning electron microscope (FEG-SEM) equipped with FIB technology and a flip-stage-STEM assembly. It is a high-tech tool for complete in situ sample preparation and high-resolution analysis. The FIB is equipped with ultra-high resolution electron optics with secondary electron (SE) and backscatter electron (BSE) in-lens detectors and STEM imaging, high-resolution (field emission) ion optics (Sidewinde column), advanced control of gas chemistries including delineation and metal etching, carbon/platinum/gold/SiO_2 deposition, high-precision piezoelectric specimen stage having a 100 mm stroke along the x- and y-axes, an *in-situ* nano-manipulator (Omniprobe, AutoProb 200) sample extraction system for lift-out TEM specimen preparation, and flip-stage pivoting TEM grid mount.

SI References

1. Kabalah-Amitai, L.; Mayzel, B.; Kauffmann, Y.; Fitch, A. N.; Bloch, L.; Gilbert, P. U. P. A.; Pokroy, B., Vaterite crystals contain two interspersed crystal sructures. *Science* **2013,** 340, 454-457.
2. Kabalah-Amitai, L.; Mayzel, B.; Zaslansky, P.; Kauffmann, Y.; Clotens, P.; Pokroy, B., Unique crystallographic pattern in the macro to atomic structure of *Herdmania momus* vateritic spicules. *J Struct Biol* **2013,** 183, 191-198.
3. Gilbert, P. U. P. A., Photoemission spectromicroscopy for the biomineralogist. In *Biomineralization Handbook, Characterization of Biominerals and Biomimetic Materials*, DiMasi, E.; Gower, L. B., Eds. CRC Press: Boca Raton, FL, 2014; pp 135-151.
4. Gilbert, B.; Andres, R.; Perfetti, P.; Margaritondo, G.; Rempfer, G.; De Stasio, G., Charging phenomena in PEEM imaging and spectroscopy. *Ultramicroscopy* **2000,** 83, 129-139.

5. De Stasio, G.; Frazer, B. H.; Gilbert, B.; Richter, K. L.; Valley, J. W., Compensation of charging in X-PEEM: a successful test on mineral inclusions in 4.4 Ga old zircon. *Ultramicroscopy* **2003,** 98, 57-62.
6. Doran, A.; Church, M.; Miller, T.; Morrison, G.; Young, A. T.; Scholl, A., Cryogenic PEEM at the Advanced Light Source. *J Electr Spectrosc Rel Phenom, special issue on Photoelectron microscopy, Time-resolved pump-probe PES* **2012,** 185, 340-346.
7. GG–Macros, http://home.physics.wisc.edu/gilbert/software.htm **2015**.
8. DeVol, R. T.; Metzler, R. A.; Kabalah-Amitai, L.; Pokroy, B.; Politi, Y.; Gal, A.; Addadi, L.; Weiner, S.; Fernandez-Martinez, A.; Demichelis, R.; Gale, J. D.; Ihli, J.; Meldrum, F. C.; Blonsky, A. Z.; Killian, C. E.; Salling, C. B.; Young, A. T.; Marcus, M. A.; Scholl, A.; Doran, A.; Jenkins, C.; Bechtel, H. A.; Gilbert, P. U. P. A., Oxygen spectroscopy and Polarization-dependent Imaging Contrast (PIC)-mapping of calcium carbonate minerals and biominerals. *The Journal of Physical Chemistry B* **2014,** 118, 8449-8457.
9. Gilbert, P. U. P. A.; Young, A.; Coppersmith, S. N., Measurement of c-axis angular orientation in calcite (CaCO3) nanocrystals using x-ray absorption spectroscopy. *Proc Natl Acad Sci USA* **2011,** 108, 11350-11355.
10. Foltz, K. R.; Adams, N. L.; Runft, L. L., Echinoderm eggs and embryos: procurement and culture. *Meth. Cell Biol.* **2004,** 74, 39-74.